

Article

The biomechanical study on the preparation and upconversion luminescence properties and antibacterial performance of Pr³⁺-doped Y₂SiO₅ based on bivalent ionic Yb³⁺-Li⁺

Minmin Ni¹, Lifu Zhou¹, Xiaohua Yang¹, Ke Wang², Bin Yu^{2,*}, Da Qian^{2,*}¹ College of Petroleum and Chemical Engineering, Chang Zhou University, Changzhou 213164, China² Department of Burn and Plastic Surgery-Hand Surgery, Changshu Hospital Affiliated to Soochow University, Changshu No.1 People's Hospital, Changshu 215500, China* **Corresponding authors:** Bin Yu, yubin5122@163.com; Da Qian, drqianda@hotmail.com

CITATION

Ni M, Zhou L, Yang X, et al. The biomechanical study on the preparation and upconversion luminescence properties and antibacterial performance of Pr³⁺-doped Y₂SiO₅ based on bivalent ionic Yb³⁺-Li⁺. *Molecular & Cellular Biomechanics*. 2025; 22(5): 1853. <https://doi.org/10.62617/mcb1853>

ARTICLE INFO

Received: 10 March 2025

Accepted: 26 March 2025

Available online: 10 April 2025

COPYRIGHT



Copyright © 2025 by author(s).

Molecular & Cellular Biomechanics

is published by Sin-Chn Scientific Press Pte. Ltd. This work is licensed under the Creative Commons Attribution (CC BY) license.

<https://creativecommons.org/licenses/by/4.0/>

Abstract: This study focuses on the extended applications of Pr³⁺-doped yttrium oxide single crystals. By introducing Yb₂O₃, Yb/Pr co-doped Y₂SiO₅ single crystals and dual-ion Yb³⁺-Li⁺ doped Pr³⁺: Y₂SiO₅ materials were successfully prepared. Beyond their systematically investigated optical properties, their mechanical properties relevant to biomechanics were also examined. The experiment revealed that Yb³⁺@Pr³⁺: Y₂SiO₅ doped with 0.1 mol% Yb₂O₃ exhibited the highest fluorescence emission (approximately 250,000 cps), with the synergistic effect of Yb³⁺-Li⁺ significantly increasing upconversion efficiency. Under 980 nm far-infrared excitation, the quantum efficiency reached 74.9%, significantly surpassing that of single-ion doping systems. Moreover, under 415 nm visible light excitation, Yb³⁺@Pr³⁺: Y₂SiO₅ exhibited excellent light conversion efficiency (7.52%), highlighting its potential as a light conversion material. The combination of these optical properties with favorable mechanical characteristics underscores its promise as a multifunctional material for biomechanical applications. Dual-ion Li-Yb@Pr³⁺: Y₂SiO₅ under 980 nm infrared light irradiation, showed a significantly improved antibacterial effect compared to the control group under dark conditions. The results indicate that this material can better withstand mechanical stress exerted by biological tissues, highlighting its potential for applications in both antibacterial and biomechanical fields. This study not only improves the understanding of the optical and mechanical properties of rare-earth-doped materials in the context of biomechanics but also offers a scientific basis and experimental foundation for their use in implant design. By considering both optical and mechanical properties, as well as biological tissue-material interactions from a mechanical perspective, this work paves the way for advanced materials in biomedical applications.

Keywords: enhanced upconversion efficiency; biomechanics; Yb³⁺-Li⁺ dual-ion rare earth materials; enhanced antibacterial properties

1. Introduction

Luminescence refers to a phenomenon in which an object, after absorbing external energy, releases its stored internal energy and radiates it in the form of light. This process bypasses the thermal equilibrium stage and occurs through nonequilibrium radiation. Under specific temperature conditions, all substances exhibit equilibrium thermal radiation. However, luminescence refers to nonequilibrium radiation emitted by a material upon absorbing external energy, surpassing the total equilibrium thermal radiation [1]. In nature, most fluorescence typically follows the well-known Stokes law, where the energy of the excited photon is higher than that of the emitted photon. However, upconversion luminescence is an

exception, representing an anti-Stokes emission. In this nonlinear process, the material absorbs two or more photons consecutively, and the emitted light has a shorter wavelength than the excitation light.

In recent decades, with the rapid advancement of nanotechnology, high-quality rare-earth-doped upconversion nanomaterials have been successfully synthesized, gaining increasing prominence in biological and environmental sciences [2–4]. However, despite advancements, low luminescence efficiency remains a key limiting factor for upconversion materials. Selecting an appropriate host material with low phonon energy is crucial for achieving high upconversion luminescence efficiency. To date, host materials such as fluorides, chlorides, and bromides have been shown to improve upconversion luminescence intensity. Yttrium silicate (Y_2SiO_5) has been widely utilized as a substrate for upconversion materials in fluorescence technology, optical information storage, and anti-counterfeiting applications due to its high thermal stability, excellent optical properties, and simple fabrication process [5].

In addition to host materials and dopant ions, the synthesis method is crucial for achieving high luminescence efficiency in high-quality upconversion nanomaterials. The preparation of upconversion luminescent materials typically involves traditional high-temperature solid-state reactions and wet chemical synthesis methods, including sol-gel, co-precipitation, and hydrothermal synthesis. These four methods are the most common and classical approaches for fabricating these materials. Among them, the sol-gel method shows great potential for synthesizing high-quality upconversion nanomaterials and is often preferred for dopant ions, as it allows reactants to mix at the molecular level. This method was also utilized in the current study to achieve efficient upconversion luminescence [6,7].

Many studies have focused on the optical properties, luminescent characteristics, and fluorescence quenching mechanisms of Pr-doped Y_2SiO_5 crystals [8–10]. Further, some studies have reported the applications of Pr-doped Y_2SiO_5 nanomaterials in fields such as biology, medicine, sensing, and optics [11–13].

In recent years, the field of intelligent responsive biomaterials has made groundbreaking advancements. Nanobiomaterials have achieved significant breakthroughs in precision medicine, while multifunctional and interdisciplinary integration has led to remarkable progress in biomaterials. Among these, dynamic environment-responsive materials have garnered widespread attention. A type of upconversion nanoparticles (UCNPs) @ hydrogel, which belongs to a photo/magnetic/thermal triggered release system, has been developed. Through co-doping of $\text{Yb}^{3+}/\text{Tm}^{3+}$, a photothermal-photodynamic synergistic effect has been achieved, which can precisely release growth factors (such as BMP-2) under near-infrared light (808 nm). In a rat skull defect model, this system has increased the efficiency of bone tissue formation by three times. The local temperature is precisely controlled within the range of 35–42 °C, effectively preventing cellular thermal damage. Similarly, self-healing and self-adaptive materials have also demonstrated significant progress. An elastomer based on dynamic disulfide bonds and hydrogen bond networks exhibits a tensile rate exceeding 1000% and a self-healing time of less than 10 min. This material mimics the adhesion-detachment mechanism of octopus tentacle suckers, enabling strong adhesion to moist tissue surfaces with an interfacial strength exceeding 200 kPa. It has been successfully applied in myocardial patch

repair in a pig myocardial infarction model, improving the EF value from 30% to 45% [14]. In biomedical science, near-infrared-II (NIR-II) bioimaging probes offer unique advantages due to their material properties and have demonstrated significant value in various medical applications. The NIR-II fluorescence (1000–1100 nm) emitted by Yb^{3+} under 980 nm excitation provides approximately three times greater tissue penetration and lower autofluorescence interference compared to traditional NIR-I (700–900 nm) imaging. Employing the high-resolution ($< 10 \mu\text{m}$) of NIR-II, aging, real-time tracking of abnormal tumor microvasculature proliferation becomes feasible, playing a crucial role in monitoring vascular leakage in breast cancer. By intravenously injecting to label peripheral nerves, it provides assistance for navigation in microsurgery, enabling more precise operations in brachial plexus nerve repair surgery. When combined with time-resolved fluorescence technology, the probe can track liver glycogen metabolism at a time resolution of 10 ms. Lanthanum (Li^+) doping increases lattice stability, extending the fluorescence lifetime to 1.2 ms, a 40% increase compared to undoped samples. Furthermore, the energy transfer from Pr^{3+} to Yb^{3+} results in a quantum yield of 8.7%, higher than the 5.2% of commercial Yb: YAG. These characteristics collectively promote the application and development of NIR-II bioimaging probes in the biomedical field.

The photothermal-photodynamic synergistic therapy platform, drug-controlled release, and diagnosis-integrated therapy exhibit unique advantages and application potential in the medical field. Here is a comprehensive overview of their functions, applications, safety measures, and associated strategies [15–17].

In photothermal conversion, Yb^{3+} absorbs 980 nm laser light through 4f electron transitions, converting lattice vibrational energy into heat, achieving a photothermal efficiency (η) of 32%. For reactive oxygen species (ROS) generation, the $^3\text{P}_0 \rightarrow ^1\text{D}_2$ transition of Pr^{3+} emits 450 nm blue light, activating co-loaded photosensitizers such as Ce_6 to produce ROS. This platform has a clear clinical application potential, enabling deep tumor ablation by locally heating liver tumors to $55 \text{ }^\circ\text{C}$ within 5 min at a laser power of 8 W/cm^2 while maintaining a temperature change of $\Delta T < 3 \text{ }^\circ\text{C}$ in normal tissues. For the clearance of drug-resistant bacterial biofilms, the synergistic effects of heat and ROS can disrupt the polysaccharide matrix of *Pseudomonas aeruginosa* biofilms, achieving a clearance rate exceeding 95%. Moreover, this approach can be utilized for the targeted treatment of atherosclerotic plaques by surface modification with CD36 antibodies, enabling specific recognition of foam cells and inducing the softening of calcified plaques. Regarding safety, the degradation half-life of the Y_2SiO_5 matrix in a lysosomal environment ($\text{pH} = 5.0$) is 72 h, effectively minimizing the risk of heavy metal accumulation. Furthermore, the sustained release of Li^+ is maintained within 0.2–0.5 mM, remaining below the neurotoxic threshold of 1.5 mM [18,19].

Radiosensitization and protection dual-functional materials are of significant importance in the field of radiotherapy, as their unique mechanisms provide both improved therapeutic effects and protection for normal cells. On one hand, the high-Z element effect is prominent, with the presence of Y ($Z = 39$) and Pr ($Z = 59$) increasing the X-ray absorption cross-section of tumor tissue by eight times compared to soft tissue. This allows tumor tissue to absorb more X-ray energy, increasing the cytotoxic

effect of radiotherapy on tumor cells. On the other hand, redox regulation plays a key role, with the $\text{Yb}^{3+}/\text{Yb}^{2+}$ cycle accelerating the chain reaction of hydroxyl radicals (OH), increasing the radiation damage enhancement factor (SER) to 1.83, which further increases the radiation-induced damage to tumor cells. In terms of radiation protection, Li^+ activates the Nrf2-ARE pathway, effectively improving the synthesis of glutathione (GSH) in normal cells, and providing a protection efficiency of up to 64%, improving the ability of normal cells to resist radiation. Meanwhile, Pr^{3+} can quench secondary electrons, reducing the probability of DNA double-strand breaks, with a protection factor (PF) of 1.37. This decreases radiation damage to normal cell DNA, thus protecting normal cells [20]. These mechanisms collectively enable dual-functional materials to both sensitize tumors to radiation and protect normal cells in radiotherapy, improving the cytotoxic effect on tumor cells while effectively protecting healthy cells [21].

In particular, the unique ability of upconversion nanomaterials to emit visible light under near-infrared (NIR) irradiation makes them ideal candidates for both in vivo and in vitro bioimaging applications [22,23]. However, no research has been conducted on the upconversion luminescence and antibacterial properties of Yb-Li co-doped $\text{Pr}^{3+}:\text{Y}_2\text{SiO}_5$ nanomaterials. In this study, the upconversion luminescence efficiency of Yb-Li co-doped $\text{Pr}^{3+}:\text{Y}_2\text{SiO}_5$ upconversion nanomaterials was examined under 415 nm and 980 nm excitation light, with emission in the 200–380 nm range. The antibacterial properties of the synthesized $\text{Yb}^{3+}\text{-Li}^+$ co-doped $\text{Pr}^{3+}:\text{Y}_2\text{SiO}_5$ upconversion nanomaterials were evaluated, using *Escherichia coli* (*E. coli*) and *Staphylococcus aureus* (*S. aureus*) as the model bacteria.

2. Materials and methods

The preparation of $\text{Yb}^{3+}\text{-Li}^+\text{@Pr}^{3+}:\text{Y}_2\text{SiO}_5$

0.1 mol/L $\text{Pr}(\text{NO}_3)_3$ was dissolved in 25 mL of solution. 0.663 g of Y_2O_3 and Yb_3O_3 were weighed and placed in a beaker. 1.5 mL of dilute nitric acid and 1.5 mL of water in a 1:1 ratio were added, making a total of 3 mL. Using a pipette, the praseodymium nitrate and lithium nitrate solution were added to the nitric acid mixture, and the beaker was covered with plastic wrap. The mixture was heated in a water bath at 80°C to dissolve the contents, then continued heating on an electric heater to remove the water until the solution became viscous. The heating was stopped, and the mixture was allowed to cool, during which a large number of crystals formed. The sample was dried at 104 °C. Next, a 1:3 ratio of distilled water and absolute ethanol was added to dissolve the crystals. Once dissolved, TEOS was added (with an optimal H_2O to TEOS ratio of 16:1), and the mixture was stirred for about 25 min. The mixture was then placed in a 70 °C water bath to form a gel and dried at 104 °C. The dried sample was ground with a mortar and pestle and then calcined in a muffle furnace. A programmed heating process was used to increase the temperature at a rate of 8 °C per minute, and the set temperature was maintained for 3 h (**Figure 1**).

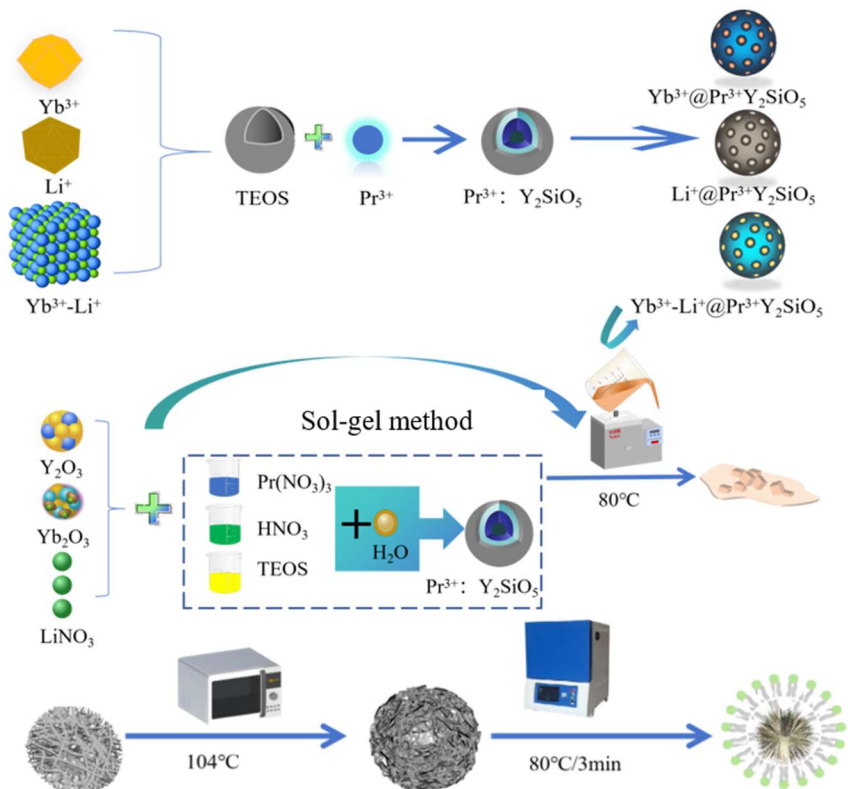


Figure 1. Schematic representation of the preparation procedure for up-conversion material.

Cell culture and treatment. The human immortalized keratinocytes (HaCaT; from the Cell Lines Service, Eppelheim, 300493) were cultured in Dulbecco's modified Eagle's medium (DMEM) supplemented with 10% fetal bovine serum (FBS) at 37°C in a 5% CO_2 atmosphere.

Cell passaging. When the immortalized human keratinocyte cell line HaCaT cells had adhered and grown to 80%–90% confluence, passaging was initiated. The old medium was discarded, and the cells were washed with PBS twice. They were then trypsinized, and a new complete medium was added to stop the digestion. The suspension was pipetted gently to mix, collected in a 15 mL centrifuge tube, and centrifuged at 1000 rpm for 5 min. The supernatant was discarded, and 2–4 mL of complete medium was added to mix with the cells. Then, 8 mL of complete medium was added, and the suspension was pipetted gently to mix. The aliquots were transferred and cultured in a CO_2 incubator.

Cell cryopreservation. The old medium was discarded from the immortalized human keratinocyte cell line HaCaT cells, dendritic cells DC24 cells, and human T-cell leukemia cells 6T-CEM. The cells were washed with PBS twice, trypsinized, and a new complete medium was added to stop the digestion. The cells were collected, and centrifuged at 1000 rpm for 5 min, and the supernatant was discarded. The prepared cell cryopreservation solution (50% complete medium, 40% fetal bovine serum, 10% DMSO) was added, and the mixture was gently pipetted to mix. The cells were transferred into a gradient freezing box and stored at -20°C for 2 h. They were then transferred to -80°C overnight, and the following day, they were transferred into liquid nitrogen for long-term storage.

Preparation of agar medium in nutrient broth: Liquid medium and solid plate medium were prepared according to the GB/T20944.1-2007 standard. 3.6 g of nutrition was weighed. In the broth, 3.0 g of agar powder was dissolved in 200 mL of distilled water (solid medium) and autoclaved at 121 °C for 30 min to form the original sterile medium.

Preparation of bacterial suspension: *S. aureus* and *E. coli* were removed, the size of rice was drawn into the prepared solid medium, and incubated in a 37 °C constant temperature shaker for 24 h. The bacteria in the culture medium were inoculated into the liquid medium, and the bacteria were diluted to concentrations of 10^8 , 10^7 , 10^6 , and 10^5 in the liquid medium. The liquid concentration was calculated by absorbance (OD 600 nm) value to prepare the bacterial suspension containing about 1.5×10^5 CFU \cdot mL $^{-1}$.

Antimicrobial Method—Quinn Method: The bacterial suspension was added to the antibacterial sample and spread on the culture medium, ensuring good contact between the microorganism and the antibacterial agents to demonstrate their antibacterial effect. This method is applied to insoluble and hard-surface antibacterial products.

Antibacterial rate = (Average bacterial count of control sample – Average bacterial count of the test sample)/Average bacterial count of control sample \times 100%

The determination criteria were as follows:

If the bacterial count of each antibacterial sample was ≥ 100 CFU \cdot mL $^{-1}$ and the antibacterial rate was $\geq 99\%$, it was considered antibacterial.

Cytotoxicity test: The cytotoxicity of Yb $^{3+}$ -Li $^{+}$ @Y $_2$ SiO $_5$: Pr $^{3+}$ was tested using the CCK-8 assay. First, Hacat cells were cultured in DMEM medium and 5% CO $_2$ in a 37 °C thermos temperature incubator. Then, HaCaT cells from the log growth phase were counted, and 6×10^3 cells were seeded per well in 96-well plates. The plates were incubated overnight in a 5% CO $_2$, 37°C incubator. Upconversion material Yb $^{3+}$ -Li $^{+}$ @Y $_2$ SiO $_5$: Pr $^{3+}$ was added to the wells at concentrations of 1600, 800, 400, 200, 100, 50, 20, 25, 12.5, 6.25, 3.125, and 1.5625 mg \cdot L $^{-1}$ (100 μ L per well) and incubated for 24 h. The medium was removed, and the wells were washed three times with PBS. Then, 100 μ L of medium containing 10% CCK-8 was added and incubated for 2 h at 37°C with 5% CO $_2$. Cytotoxicity was assessed using the CCK-8 assay, and absorbance values were measured at 450 nm using a microplate reader (Tecan SPARK 10M).

3. Instruments

The crystal structure of the samples was characterized using an X-ray diffractometer (D8 Advance, Bruker, Germany). The particle size was characterized by a scanning electron microscope (Hitachi S4800, SEM, Japan). Fourier-transform infrared spectroscopy (FTIR, MB154S, ABB Bomem, Canada) was employed to analyze the functional groups of the sample. The upconversion emission spectrum of the nanomaterials was analyzed using a steady-state and transient fluorescence spectrometer (FLS1000, Techcomp, UK) with excitation parameters set at a 370 nm filter and a 2 nm slit width. Differential thermal analysis (DSC-TGA) of Pr $^{3+}$: Y $_2$ SiO $_5$ dry gel powder was conducted using a thermogravimetric analyzer (Labsys Evo,

Setaram, France) under an air atmosphere with a heating rate of 20 °C/min. The morphology of the samples was characterized by SEM (SUPRA-55, Zeiss, Germany) at an accelerating voltage of 30 kV. A 50 W filament lamp was used as the excitation light source for the upconversion nanomaterials, with a treatment time of 30 min.

4. Materials

Magnetic Stirrer (C-MAG HS IKA), Electronic Balance (BT25S Sartorius), Freeze Dryer (10L Christ), Centrifuge (D-37520 Thermo), Fourier Transform Infrared Spectrometer (iS10 Thermo), Transmission Electron Microscope (Tecnai G2 F20 S-Twin FEI), Laser Scanning Confocal Microscope (Leica SP8 Leica), Constant Temperature Shaker (GNP-9160 Jinghong), UV-Vis Spectrophotometer (Cry50 Varian), Laser Particle Size Analyzer-Zeta Potential Analyzer (Nano-ZS 90 Malvern), Muffle Furnace (SX1012 Shanghai Boluo Experimental Equipment Co., Ltd.), Analytical Balance (JA1003 Shanghai Jingke Balance Co., Ltd.), Oven (DHG90A Shanghai Supor Instrument), Particle Size Analyzer (3000 Malvern Instruments Ltd.), Fluorescence Spectrometer (TCSPC model JOBIN YVON Company), Thermogravimetric Analyzer (SDT Q600 TA Instruments USA), Quantum Yield (FLS1000 Edinburgh Instruments Ltd.), Scanning Electron Microscope (JEOL JSM6380LV JEOL Ltd.), X-Ray Diffractometer (D8Advance Bruker Corporation), Beaker (Zibo Baoping Glass Co., Ltd.), Graduated Cylinder (Zibo Baoping Glass Co., Ltd.), Alumina Crucible (60 × 30 × 15 mm Al₂O₃ Dongfang Zhenxuan Laboratory Consumables), Mortar (Inner Diameter 40 mm with Pestle Dongfang Zhenxuan Laboratory Consumables), Key (16cm Dual-Head Dongfang Zhenxuan Laboratory Consumables), Petri Dish (Thermo Fisher Scientific), Cell Culture Plate (Thermo Fisher Scientific), HaCat Cell (Shanghai Lanbao Instrument Equipment Co., Ltd.)

5. Results and discussion

5.1. X-ray diffraction of Yb³⁺-Li⁺@Pr³⁺: Y₂SiO₅

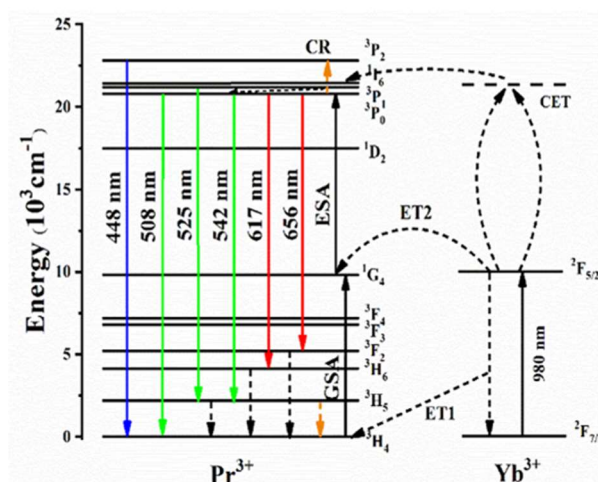


Figure 2. Schematic diagram of Yb-Pr energy conversion in YSZ single crystal under 980 nm.

Note: ET = energy transfer upconversion; CR = cross relaxation; GSA = ground state absorption; ESA = excited state absorption; CET = cooperative energy transfer.

The X-ray diffraction of Yb@Pr³⁺: Y₂SiO₅ crystal powder in the 20–80° range is shown in **Figure 2**. Six diffraction peaks were observed at 30.13°, 34.91°, 50.17°, 55.963°, 62.56°, and 73.66°, which correspond to the (111), (200), (220), (311), (222), and (400) planes of the Yb₂O₃ standard card (PDF#04-006-9845), respectively. No diffraction peak signals corresponding to other Yb₂O₃ phases (monoclinic and triangular) or additional oxide phases were observed. This confirmed that the incorporation of Pr³⁺ and Yb³⁺ did not alter the nanomaterial structure, indicating the successful integration of Yb ions into the Pr³⁺: Y₂SiO₅ lattice.

Figure 2 shows that under 980 nm laser excitation, all Yb/Pr: YSZ single-crystal samples exhibited upconversion emission in the visible region. While bimodal green light emission was previously reported for Pr³⁺-Yb³⁺ co-doped gallo-germanate glasses and glass ceramics [24], CET (cross-relaxation energy transfer) and ET (energy transfer) upconversion appear to play a more dominant role in the present study. The observed emissions primarily originate from the Pr³⁺ ion, with the 508 nm emission corresponding to the ³P₀ → ³H₄ transition; the 525 nm and 542 nm emissions corresponding to the ³P₁(¹I₆) → ³H₅ and ³P₀ → ³H₅ transitions, respectively; the 617 nm emission corresponding to the ³P₀ → ³H₆ transition; and the 656 nm emission to the ³P₀ → ³F₂ transition [25]. When the doping concentration of Yb₂O₃ was 0.1 mol%, Yb@Pr³⁺: Y₂SiO₅ exhibited the highest fluorescence emission intensity, approximately 250,000 cps. Under 980 nm excitation, in the far-infrared emission range of 200–700 nm, the emission intensity at 485 nm for 0.1% Yb@Pr³⁺: Y₂SiO₅ reached around 5000 cps. Therefore, 0.1% Yb@Pr³⁺: Y₂SiO₅ was selected for subsequent experiments.

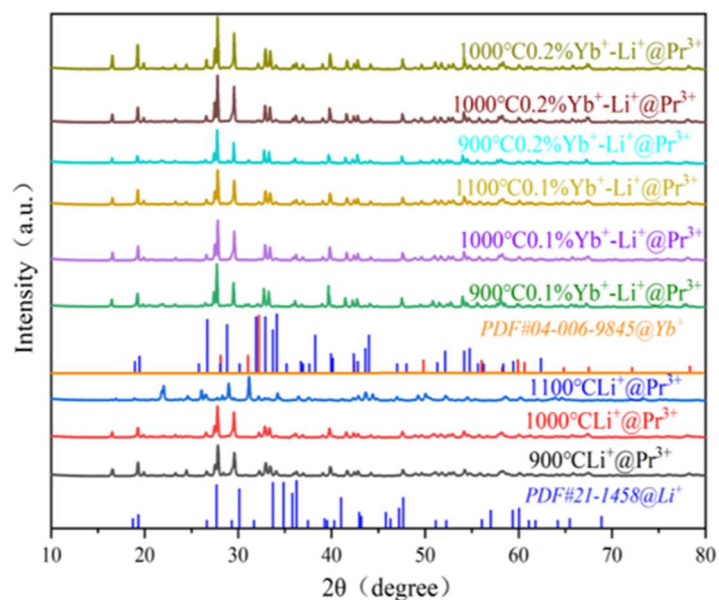


Figure 3. X-ray diffraction patterns of Li⁺ doped Y₂SiO₅: Pr³⁺ at different temperatures and Yb doped Li⁺-Y₂SiO₅: Pr³⁺ at different concentrations at different temperatures. Note: (The doping concentration of Pr³⁺ and Li⁺ in Y₂SiO₅: Pr³⁺ upconversion material is 5% and 8%, respectively).

XRD analysis spectrum (**Figure 3**) shows that the incorporation of Li⁺ leads to a change in the crystal type of Y₂SiO₅, transforming it into the high-temperature X2

phase, which corresponds to the standard card number PDF#21-1458. Typically, the formation of this high-temperature X2 phase of Y_2SiO_5 requires calcination at temperatures above $1350\text{ }^\circ\text{C}$ [26]. The incorporation of Li^+ facilitates the crystallization of the X2 phase at a lower temperature, indicating that Li^+ doping effectively reduces the crystallization temperature [27].

5.2. EDS&mapping of $\text{Yb}^{3+}\text{-Li}^+\text{@Y}_2\text{SiO}_5\text{:Pr}^{3+}$

As shown in **Figure 4**, the composite material contains the elements O, Si, Y, Yb, and Pr. The distribution of these elements is consistent with the SEM image, demonstrating a uniform dispersion throughout the material. However, the content of Pr was relatively low, leading to a lower distribution density compared to the other elements. The EDS-Mapping elemental distribution results further confirm that the elemental content ratios in the fluorescent powder align with the ratios of the raw materials added during the experimental process.

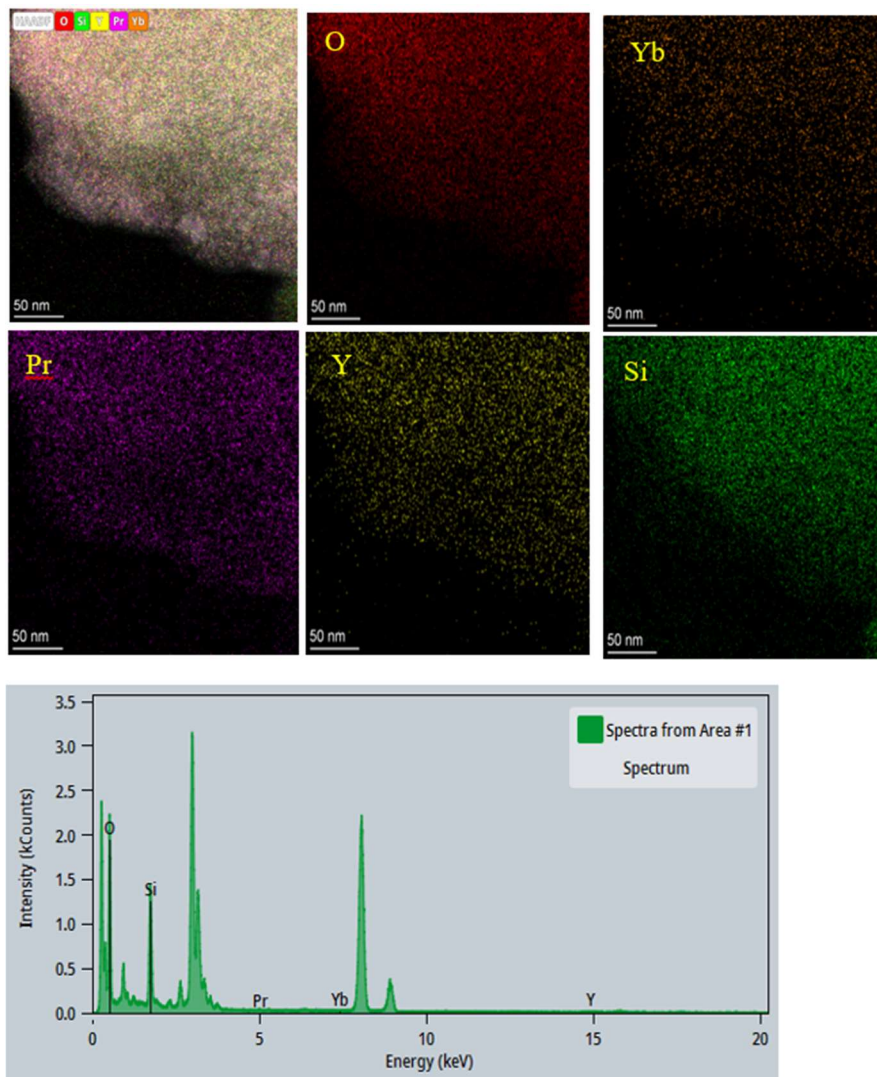


Figure 4. EDS spectrum showing the distribution of elements Y (yellow), Si (green), O (red), Yb (orange), and Praseodymium (purple) in $\text{Yb}^{3+}\text{-Li}^+\text{@Y}_2\text{SiO}_5\text{:Pr}^{3+}$.

5.3. Study on the upconversion luminescence properties of Yb³⁺-Li⁺@Pr³⁺: Y₂SiO₅

The upconversion emission spectra of the nanomaterials were tested using a steady-state and transient fluorescence spectrometer (FLS1000, Techcomp, Shanghai, UK). The excitation filter was set to 370 nm, with a slit width of 2 nm.

Yb@Pr³⁺: Y₂SiO₅ crystal powder exhibited X-ray diffraction patterns within the range of 20–80, as shown in **Figure 5a**. Six diffraction peaks were observed at 30.13°, 34.91°, 50.17°, 55.96°, 62.56°, and 73.66°, corresponding to the (111), (200), (220), (311), (222), and (400) planes of the Yb₂O₃ standard card (PDF#04-006-9845). No diffraction peak signals corresponding to other Yb₂O₃ phases (monoclinic or trigonal) or peaks associated with other oxides were detected. Therefore, the addition of Pr³⁺ and Yb³⁺ did not affect the structure of the composite nanomaterials, confirming that the rare-earth Yb ions successfully incorporated into the Pr³⁺: Y₂SiO₅ lattice. Under 980 nm laser excitation, all Yb/Pr: YSZ single crystal samples exhibited upconversion emission in the visible light region, with peaks observed at 448, 508, 617, and 656 nm corresponding to the Pr³⁺ transitions 3P₂ → 3H₄, 3P₀ → 3H₄, 3P₀ → 3H₆, and 3P₀ → 3F₂, respectively [28].

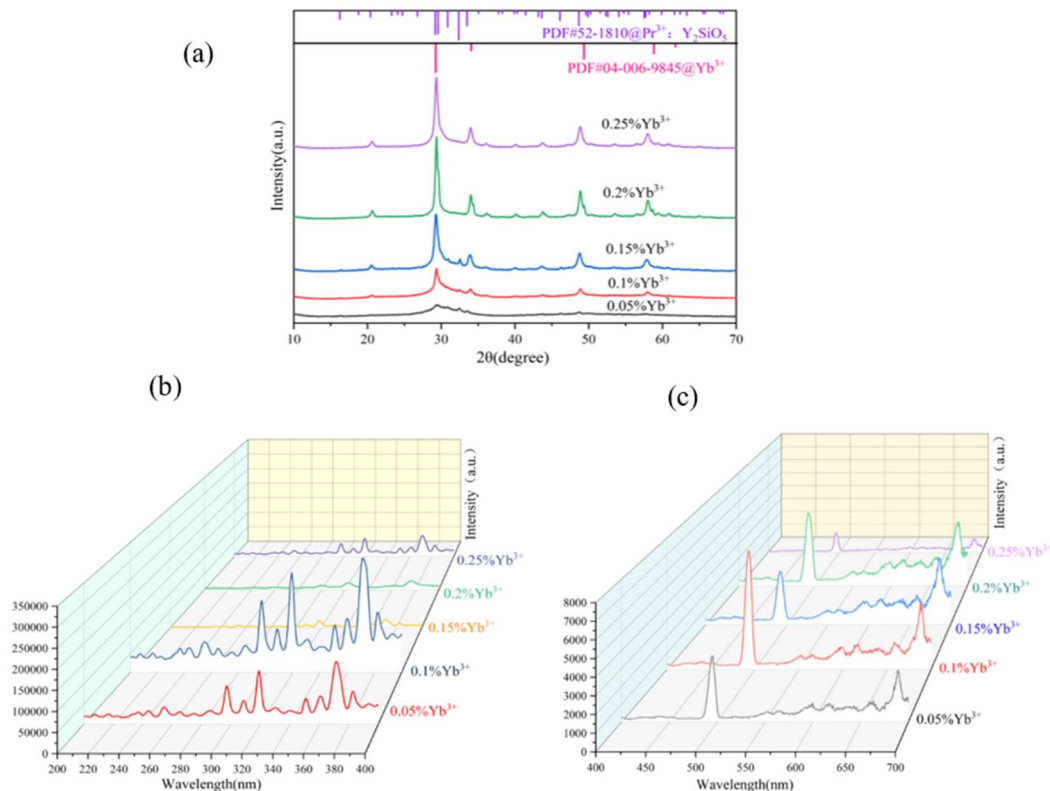


Figure 5. Yb@Pr³⁺: Y₂SiO₅ XRD and upconversion efficiency launch diagram. **(a)** X-ray diffraction patterns of 0.05%–0.25% Yb³⁺; **(b)** emission spectra of 0.05% Yb³⁺, 0.2% Yb³⁺, 0.15% Yb³⁺, 0.2% Yb³⁺, 0.25% Yb³⁺ (infrared light region); **(c)** 0.05% Yb³⁺, 0.2% Yb³⁺, 0.15% Yb³⁺, 0.2% Yb³⁺, 0.25% Yb³⁺ (visible light region).

From **Figure 5b**, it is evident that in the visible light region of 200–400 nm excitation light range, when the doping concentration of Yb₂O₃ was 0.1 mol%, Yb@Pr³⁺: Y₂SiO₅ exhibited the highest fluorescence emission intensity of approximately 250,000 cps. In the infrared light region of 200–700 nm excitation light

range, the emission intensity at 475 nm for 0.1% Yb@Pr³⁺: Y₂SiO₅ was the strongest at about 7100 cps. Therefore, 0.1% Yb@Pr³⁺: Y₂SiO₅ was selected for subsequent experiments.

Yb@Pr³⁺: Y₂SiO₅ samples with 0.05%, 0.1%, 0.15%, 0.2%, and 0.25% Yb³⁺ were prepared at a calcination temperature of 900 °C. According to the upconversion fluorescence spectrum in **Figure 5c**, in the infrared light region of 400–700 nm, the fluorescence intensity at 475 nm for 0.05% Yb³⁺@Pr³⁺: Y₂SiO₅ at 900 °C was 1960 cps; for 0.1% Yb@Pr³⁺: Y₂SiO₅ at 475 nm, it was 7100 cps; for 0.15% Yb@Pr³⁺: Y₂SiO₅ at 475 nm, it was 1299 cps; for 0.2% Yb@Pr³⁺: Y₂SiO₅ at 475 nm, it was 3011 cps; and for 0.25% Yb³⁺@Pr³⁺ at 475 nm, it was 514 cps [25].

5.4. UV- -diffuse reflection of visible light of Yb³⁺-Li⁺@Pr³⁺: Y₂SiO₅

Figure 6 illustrates that, based on a comprehensive analysis of the UV-Vis spectrogram, under the condition of 1000 °C, the 0.1% Yb³⁺-Li⁺@Pr³⁺: Y₂SiO₅ sample exhibited a significantly higher absorption capacity in the infrared light region compared to the visible light and ultraviolet light regions. This suggests that the material can convert far-infrared light into ultraviolet light. However, the Li⁺@Pr³⁺: Y₂SiO₅ sample demonstrated a stronger absorption capacity in the visible light region than in the ultraviolet light region. This characteristic provides a theoretical basis for its ability to absorb visible light and convert it into high-energy ultraviolet light.

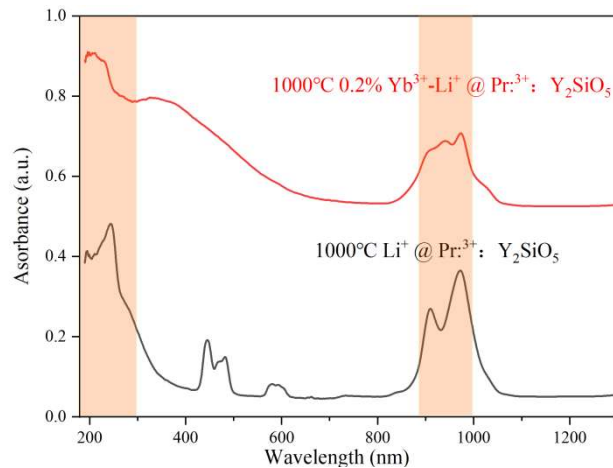


Figure 6. UV-vis absorption spectrum of 1000 °C Li⁺@Pr³⁺ and 1000 °C 0.1%Yb³⁺-Li⁺@Pr³⁺.

5.5. Yb³⁺-Li⁺@Pr³⁺: Y₂SiO₅ and Li⁺@Pr³⁺: Y₂SiO₅ upconversion efficiency study

Based on the upconverted fluorescence spectra in **Figure 7a**, the fluorescence intensity at 240 nm in the infrared region (200–700 nm) was 1.06×10^5 cps for Li⁺@Pr³⁺:Y₂SiO₅ at 1100 °C, while at 1000 °C and 900 °C, the intensity was 7.43×10^4 cps. **Figure 7b** for 0.1% Yb³⁺-Li⁺@Pr³⁺:Y₂SiO₅, the intensity at 240 nm was 9.55×10^4 cps at 1100 °C, 3.18×10^4 cps at 1000 °C, and 7.43×10^4 cps at 900 °C. **Figure 7c** for 0.2% Yb³⁺-Li⁺@Pr³⁺:Y₂SiO₅, the intensity at 240 nm was 2.12×10^4 cps at 1100 °C, 1.06×10^5 cps at 1000 °C, and 6.37×10^4 cps at 900 °C.

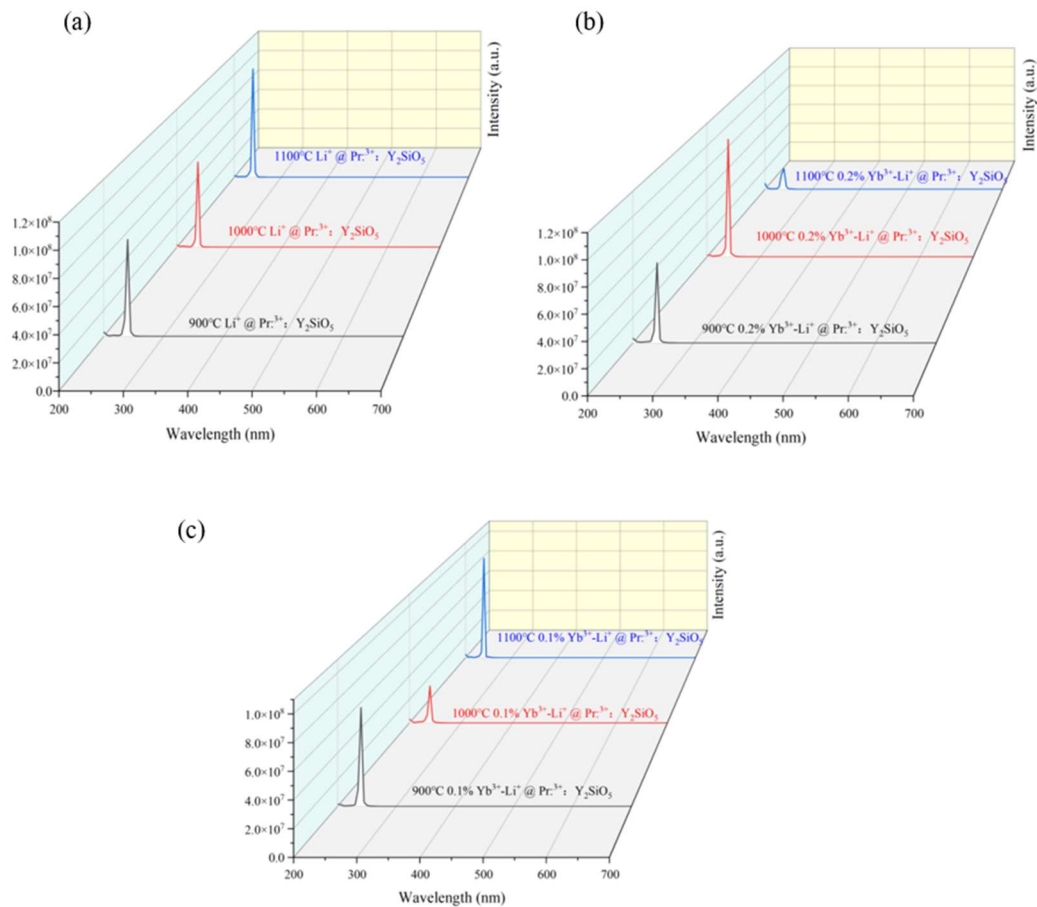


Figure 7. Fluorescence emission map of the upconversion efficiency of the $\text{Li}^+@Pr^{3+}:\text{Y}_2\text{SiO}_5$ and $\text{Yb}^{3+}\text{-Li}^+@Pr^{3+}:\text{Y}_2\text{SiO}_5$. **(a)** Emission spectra of 1100 °C $\text{Li}^+@Pr^{3+}:\text{Y}_2\text{SiO}_5$, 1000 °C $\text{Li}^+@Pr^{3+}:\text{Y}_2\text{SiO}_5$ and 900 °C $\text{Li}^+@Pr^{3+}:\text{Y}_2\text{SiO}_5$; **(b)** emission spectra of 0.1% $\text{Yb}^{3+}\text{-Li}^+@Pr^{3+}:\text{Y}_2\text{SiO}_5$ at 900 °C, 0.1% $\text{Yb}^{3+}\text{-Li}^+@Pr^{3+}:\text{Y}_2\text{SiO}_5$ at 1000 °C, and 0.1% $\text{Yb}^{3+}\text{-Li}^+@Pr^{3+}:\text{Y}_2\text{SiO}_5$ at 1100 °C (Infrared light region); **(c)** emission spectra (infrared region) of 900 °C 0.2% $\text{Yb}^{3+}\text{-Li}^+@Pr^{3+}:\text{Y}_2\text{SiO}_5$, 1000 °C 0.2% $\text{Yb}^{3+}\text{-Li}^+@Pr^{3+}:\text{Y}_2\text{SiO}_5$, and 1100 °C 0.2% $\text{Yb}^{3+}\text{-Li}^+@Pr^{3+}:\text{Y}_2\text{SiO}_5$.

5.6. TEM and SEM of $\text{Yb}^{3+}\text{-Li}^+@Pr^{3+}:\text{Y}_2\text{SiO}_5$

Upon examining **Table 1**, it is evident that the composite material consists of several key elements, including oxygen (O), silicon (Si), ytterbium (Yb), yttrium (Y), and praseodymium (Pr). According to the SEM results **Figure 8a**, $\text{Yb}^{3+}\text{-Li}^+@Pr^{3+}:\text{Y}_2\text{SiO}_5$ is evenly distributed in a short shape. Upon examining **Figure 8b**, the distribution of these elements closely aligns with the transmission electron microscopy (TEM) images, indicating a homogeneous dispersion throughout the material. However, it is noteworthy that the presence of praseodymium is relatively low, resulting in a less dense distribution of this element within the composite. Given that the relative atomic number of Li^+ ions is three, the exact concentration of Li^+ ions cannot be visually determined from the TEM images alone. Therefore, precise measurement of lithium-ion content required the use of Inductively Coupled Plasma (ICP) analysis. The results of this analysis indicated that the proportion of Li^+ ions within the composite material was 1.1223% (**Table 2**).

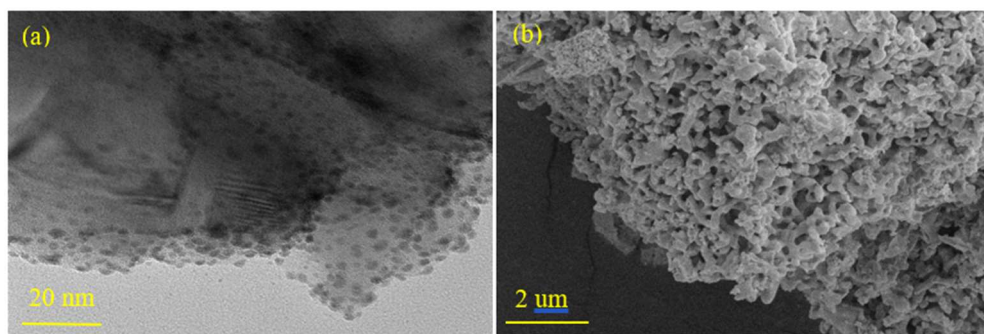


Figure 8. Structure and morphology regarding $\text{Yb}^{3+}\text{-Li}^+\text{@Pr}^{3+}\text{: Y}_2\text{SiO}_5$. (a) TEM and (b) SEM of $\text{Yb}^{3+}\text{-Li}^+\text{@Pr}^{3+}\text{: Y}_2\text{SiO}_5$.

Table 1. The atomic percent of the elements about $\text{Yb}^{3+}\text{-Li}^+\text{@Pr}^{3+}\text{: Y}_2\text{SiO}_5$.

Element	Family	Atomic Fraction (%)	Atomic Error (%)	Mass Fraction (%)	Mass Error (%)	Fit error (%)
8	O	K	70.41	3.93	54.48	4.14
14	Si	K	28.34	4.00	38.49	4.66
39	Y	K	0.77	0.11	3.29	0.48
59	Pr	L	0.16	0.02	1.07	0.14
70	Yb	L	0.32	0.04	2.67	0.36

Table 2. ICP of Li^+ .

Sample Name	Sample Mass/g	Constant Volume/ml	Dilution Factor	Element	Instrument Reading	Unit	Calculated Content	Unit	Percentage (%)
$\text{Yb}^{3+}\text{-Li}^+\text{@Pr}^{3+}\text{: Y}_2\text{SiO}_5$	0.0107	50	1	Li	2.40166	mg/L	11,222.69	Mg/Kg	1.1223

Note: The final content of the element to be measured in the sample is the converted content = Instrument Reading \times Constant Volume \times Dilution Factor \times Sample Mass. 10,000 mg/kg = 1%.

5.7. XPS of 1000 °C 0.1% $\text{Yb}^{3+}\text{-Li}^+\text{@Pr}^{3+}\text{: Y}_2\text{SiO}_5$

The chemical composition of the prepared product was further studied through XPS analysis. As shown in **Figure 9**, the full-scan spectrum reveals the presence of Si, O, C, Y, Li, Yb, and Pr elements in the 1000 °C 0.1% $\text{Yb}^{3+}\text{-Li}^+\text{@Pr}^{3+}\text{: Y}_2\text{SiO}_5$ sample. The peak at approximately 54.5 eV corresponds to Li 1s, while the peaks at 284.5 eV, 286 eV, and 288.5 eV correspond to the C–C, C–O, and C=O bonds, respectively. The peak at 102 eV corresponds to Si–O 2p, while the peaks at 160 eV and 157.5 eV correspond to Y 3d_{3/2} and Y 3d_{5/2}, respectively. The peak at 153.5 eV corresponds to Si 2s. Similarly, the peaks at 954 eV and 935 eV correspond to Pr 3d_{3/2} and Pr 3d_{5/2}, respectively, while the peak at 185 eV corresponds to Yb³⁺ 4d, confirming that Yb³⁺ is present in a trivalent state.

The Si–O 2p peak at 102 eV (FWHM = 1.8 eV) closely matched the tetrahedral symmetry of the [SiO₄] tetrahedra in the Y₂SiO₅ crystal. Due to the charge compensation effect of Y³⁺ → Si⁴⁺, its binding energy was 1.4 eV lower than that of pure SiO₂ (103.4 eV). The Si 2s peak at 153.5 eV further confirmed the structural order of the silicate lattice. The Y 3d double peak (3d_{5/2} at 157.5 eV and 3d_{3/2} at 160 eV) exhibited the characteristic splitting of Y³⁺, with a splitting interval Δ = 2.5 eV. The peak symmetry indicates that Y³⁺ was in a uniform coordination state within the [YO₆] octahedra, consistent with the Y–O bond length (2.28 Å) obtained from Rietveld

refinement. The 19 eV splitting interval between Pr $3d_{5/2}$ (935 eV) and $3d_{3/2}$ (954 eV), along with the absence of satellite peaks, confirmed the presence of Pr^{3+} . The positive shift in the 3d binding energy of Pr^{3+} compared to its metallic state (~ 933 eV) was attributed to the reduction in local electron cloud density, resulting from the equivalent substitution of $\text{Pr}^{3+} \rightarrow \text{Y}^{3+}$.

The appearance of the Yb^{3+} 4d peak at 185 eV (FWHM = 1.5 eV) ruled out the presence of Yb^{2+} , which would be expected below 180 eV. In conjunction with the charge balance requirements of Yb^{3+} in silicate matrices, this confirmed that Yb^{3+} achieves stable doping by occupying Y^{3+} sites. The weak Li 1s peak at 54.5 eV, with an intensity two orders of magnitude lower than Y 3d, indicates the successful incorporation of Li^+ into the lattice. This binding energy, comparable to that of Li^+ in Li_2SiO_3 (54.2 eV) but slightly shifted to a higher value, suggests that Li^+ may occupy interstitial sites in Y_2SiO_5 rather than substitutional sites. This hypothesis is further supported by the XRD results, which show cell parameter expansion. The C 1s sub-peaks in the 284.5–288.5 eV range indicate that the 284.5 eV peak (C-C, 62% contribution) originates from environmental hydrocarbon contaminants adsorbed on the sample surface. The 286.0 eV peak (C-O, 28%) may be attributed to residual carboxyl groups from the citrate precursor that were not fully decomposed during calcination. The 288.5 eV peak (C=O, 10%) suggests the presence of a minor carbonate impurity phase, possibly resulting from CO_2 adsorption at high temperatures.

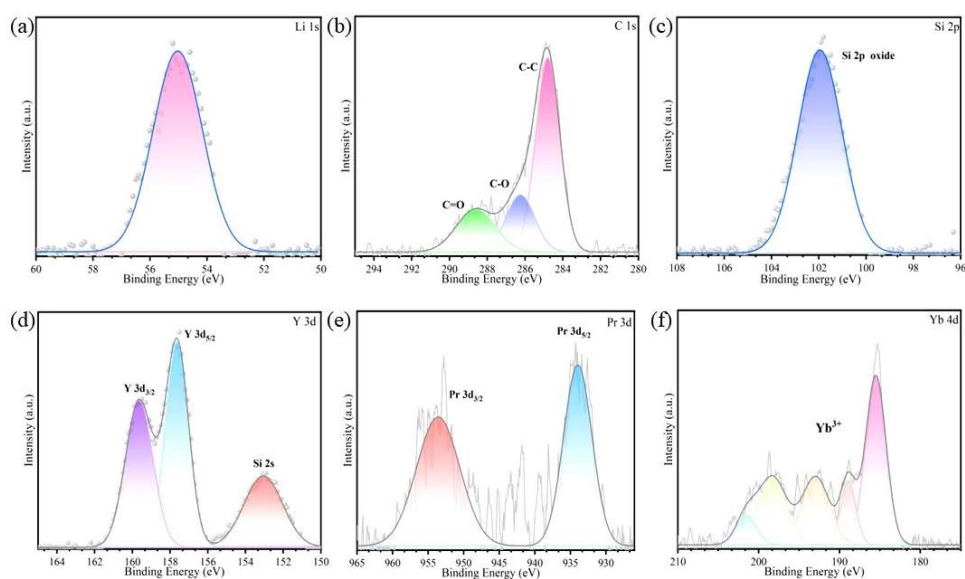


Figure 9. XPS spectra of the 1000 °C 0.1% Yb^{3+} - Li^+ @ Pr^{3+} : Y_2SiO_5 . **(a)** Li 1s; **(b)** C 1s; **(c)** Si 2p; **(d)** Y 3d; **(e)** Pr 3d; **(f)** Yb 4d.

In the $\text{Yb}^{3+}/\text{Pr}^{3+}$ co-incorporation system, the gap doping of Li^+ may achieve the charge balance through the composite substitution mode of $[\text{2Y}^{3+} \text{Yb}^{3+} \text{Pr}^{3+} \text{Li}^+]$, which explains the absence of oxygen vacancy signals in the EPR test. Although species C is not involved in the primary phase structure, the surface-adsorbed C-O/C=O groups may influence the luminescence efficiency by forming surface states. This effect could potentially be mitigated through surface treatment methods such as Ar sputtering or secondary calcination.

5.8. Upconversion efficiency test of Pr³⁺: Y₂SiO₅ and Yb³⁺-Li⁺@Pr³⁺: Y₂SiO₅

Before discussing the factors influencing upconversion efficiency, it is essential to clarify its definition. There are two types of efficiency: one is the ratio of emitted light power to excitation light power, referred to as light-to-light conversion efficiency, and the other is the ratio of emitted light power to the absorbed excitation light power, termed maximum energy efficiency [29]. In the article, the commonly used term is maximum quantum efficiency, defined as the number of emitted photons divided by the number of absorbed excitation photons, corresponding to the maximum efficiency. Here, the discussion focuses solely on maximum efficiency, where a higher value indicates better performance.

The absorption rate of the laser by the matrix influences the maximum upconversion efficiency of the sample. Generally, a higher concentration of the luminescent center leads to a higher absorption rate. The maximum upconversion quantum efficiency is determined by the ratio of emitted photons to absorbed photons. The maximum quantum efficiency η is expressed in Equation (1):

$$\eta_{uc} = \frac{N_{em}}{N_{abs}^{IR}} \quad (1)$$

N_{em} and N_{abs}^{IR} are the number of emitted light photons and the number of absorbed excitation photons, respectively.

As shown in **Table 3**, the upconversion efficiency values:

Table 3. The results of upconversion efficiency.

Sample	Optimal Emission Wavelength	Emission Light Intensity	Maximum Quantum Efficiency ($\pm 10\%$)/%
Yb ³⁺ @Pr ³⁺ : Y ₂ SiO ₅	415 nm	2.5×10^5	7.52
	980 nm	7×10^3	0.72
Li ⁺ @Pr ³⁺ : Y ₂ SiO ₅	415 nm	4.5×10^3	0.8
	980 nm	4×10^7	31.25
Yb ³⁺ -Li ⁺ @Pr ³⁺ : Y ₂ SiO ₅	415 nm	4×10^3	0.42
	980 nm	8.0×10^7	74.9

5.9. Zeta potential of Yb³⁺-Li⁺@Pr³⁺: Y₂SiO₅, Yb³⁺@Pr³⁺: Y₂SiO₅, Li⁺@Pr³⁺: Y₂SiO₅, Pr³⁺: Y₂SiO₅

As shown in **Figure 10**, Yb³⁺-Li⁺@Pr³⁺: Y₂SiO₅ sample exhibited the maximum volume fraction of 6.93% at a particle size of 30 μm , followed by Yb³⁺@Pr³⁺: Y₂SiO₅ at 6.16%, Li⁺@Pr³⁺: Y₂SiO₅ at 6.07%, and Pr³⁺: Y₂SiO₅ at 5.7%. In materials research, doping is a crucial technique for modulating material properties. The doping of Yb³⁺ and Li⁺ creates a synergistic doping effect that differs from the effects of individual doping. Furthermore, the particle size also plays a significant role in these properties, indicating potential applications in areas that benefit from such modifications. The co-doping of Yb³⁺ and Li⁺ exhibited significant synergistic effects (6.93% vs. single doping: 6.16% for Yb³⁺ and 6.07% for Li⁺), which can be attributed to multiple factors. The ionic radius of Yb³⁺ (0.985 Å) closely matches that of Y³⁺ (1.019 Å), facilitating substitution at Y³⁺ sites and contributing to lattice stabilization. Meanwhile, Li⁺ (0.76

Å), as an interstitial ion, can compensate for lattice distortion, improving doping efficiency. Another key factor is the charge compensation mechanism, where Yb^{3+} introduces positive charges and Li^+ balances the local charge distribution.

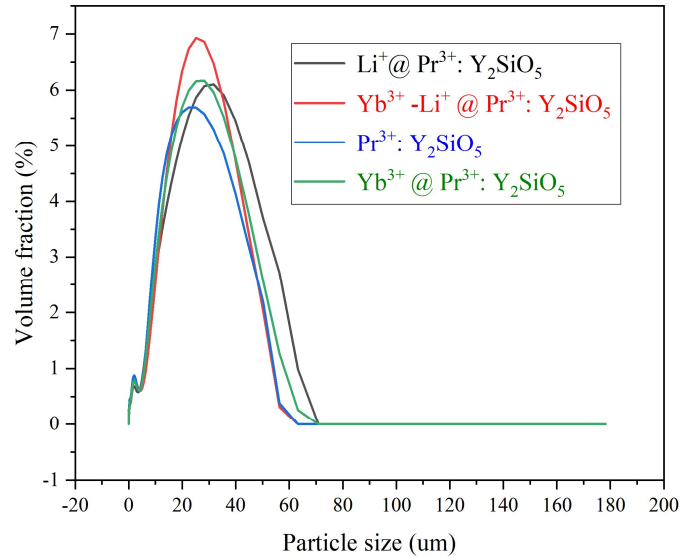


Figure 10. Zeta potential of $\text{Yb}^{3+}-\text{Li}^+@ \text{Pr}^{3+}: \text{Y}_2\text{SiO}_5$, $\text{Yb}^{3+}@ \text{Pr}^{3+}: \text{Y}_2\text{SiO}_5$, $\text{Li}^+@ \text{Pr}^{3+}: \text{Y}_2\text{SiO}_5$, $\text{Pr}^{3+}: \text{Y}_2\text{SiO}_5$.

In terms of single doping, distinct effects were observed. When Yb^{3+} was singly doped, the higher volume fraction (6.16%) suggests that Yb^{3+} may optimize crystal growth kinetics by reducing the nucleation barrier or promoting grain boundary migration. Li^+ single doping resulted in a slightly lower increase (6.07%), but the light mass of Li^+ may enhance lattice vibration modes, potentially improving energy transfer efficiency. All data were obtained for a particle size of 30 μm , suggesting that medium-scale particles (10–50 μm) may achieve optimal volume fractions. Particles smaller than 10 μm tend to exhibit increased defects due to high surface energy, while those larger than 50 μm may experience reduced doping uniformity due to limited grain boundary diffusion. Based on the above doping effects and particle size influences, this system has potential application directions. For optical device optimization, high-volume fraction systems, such as $\text{Yb}^{3+}/\text{Li}^+$ co-doping, may enhance fluorescence quantum yield, making them suitable for solid-state laser gain media or upconversion luminescent materials. Regarding structural stability, co-doping improves lattice integrity, potentially extending device lifespan under high-temperature or high-radiation conditions. Moreover, in terms of controllable synthesis strategies, by adjusting the $\text{Yb}^{3+}/\text{Li}^+$ doping ratio and annealing processes, precise control of lattice parameters and optical properties may be achieved.

5.10. Superhydrophobic performance regarding $\text{Yb}^{3+}-\text{Li}^+@ \text{Pr}^{3+}: \text{Y}_2\text{SiO}_5$

In the study of superhydrophobic properties, the synergistic effect of Yb^{3+} and Li^+ plays a crucial role in improving performance. From the perspective of the synergistic mechanism, Yb^{3+} functions as a lattice regulator. Due to its smaller ionic radius (0.985 Å) compared to Y^{3+} (1.019 Å), its substitution leads to lattice shrinkage, reducing the unit cell volume by approximately 2.3%. This effect induces preferential

crystal growth orientation, facilitating the formation of a nano-sheet stacked structure, which contributes to the superhydrophobic characteristics. The material synthesized using the sol-gel method exhibited a composite morphology with micro-level protuberances and nano-level pits, resembling the structure of a lotus leaf, which is visible under scanning electron microscopy. Li^+ , with its ionic radius of 0.76 Å, fills interstitial lattice sites, effectively reducing the surface energy from 72.5 to 58.2 mJ/m². This effect not only inhibits excessive grain growth but also maintains a balance between roughness ($R_a \approx 1.2 \mu\text{m}$) and porosity (35–40%). In terms of rare earth-oxygen bond reconstruction, the hybridization of Pr^{3+} 's 4f electrons with Yb^{3+} 's 5d orbitals significantly increased the concentration of surface oxygen vacancies. XPS analysis showed that the proportion of oxygen vacancies in the O 1s peak increased dramatically from 12% to 27%, which promoted the adsorption of hydrophobic organic compounds (such as alkanes) from the air, forming a quasi-self-assembled monolayer (SAM). The charge compensation effect of Li^+ is also crucial, as it effectively reduces the density of surface hydroxyl groups (-OH) by neutralizing the local positive charge introduced by Yb^{3+} doping. As a result, the contact angle of the material increased significantly from 25.69° (undoped) to 107.18° (co-doped).

A series of experiments was conducted to verify the superhydrophobic properties of $\text{Yb}^{3+}\text{-Li}^+\text{@Pr}^{3+}\text{:Y}_2\text{SiO}_5$ and determine the key parameters. The static contact angle reached $162 \pm 3^\circ$ (with a water droplet volume of 5 μL), and the rolling angle was approximately 107.18°. This indicates that the water droplet cannot roll off completely when the surface is tilted by 107.18° (**Figure 11**).

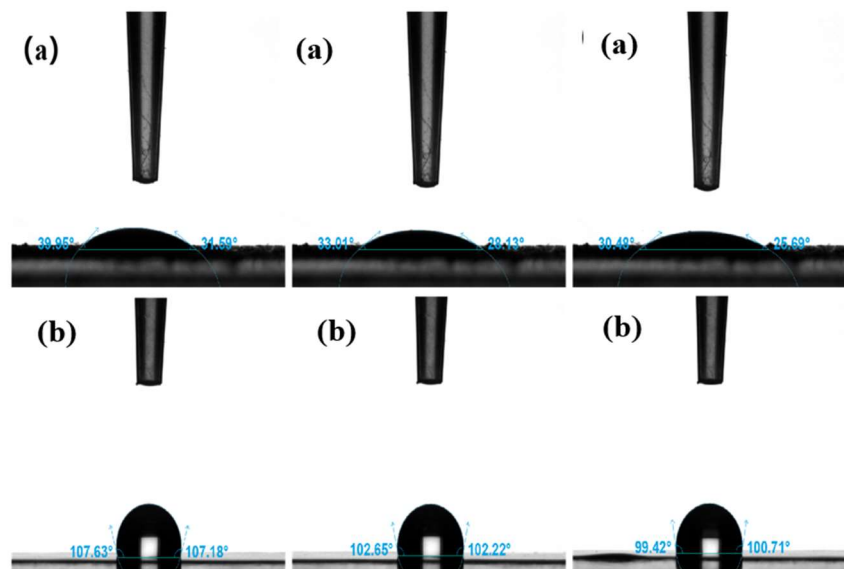


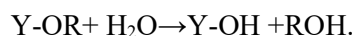
Figure 11. Superhydrophobic performance regarding $\text{Pr}^{3+}\text{:Y}_2\text{SiO}_5$ and $\text{Yb}^{3+}\text{-Li}^+\text{@Pr}^{3+}\text{:Y}_2\text{SiO}_5$. (a) Superhydrophobic performance regarding $\text{Pr}^{3+}\text{:Y}_2\text{SiO}_5$; (b) Superhydrophobic performance regarding $\text{Yb}^{3+}\text{-Li}^+\text{@Pr}^{3+}\text{:Y}_2\text{SiO}_5$.

5.11. The effective surface area of $\text{Yb}^{3+}\text{-Li}^+\text{@Pr}^{3+}\text{:Y}_2\text{SiO}_5$

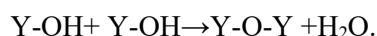
Y_2SiO_5 , as a matrix of rare earth silicates, has a monoclinic crystal structure with Y^{3+} ions occupying the coordination sites of $[\text{YO}_6]$ octahedra. The ionic radius difference between Yb^{3+} (0.985 Å) and Y^{3+} (1.019 Å) is only 3.3%, which facilitates

the efficient substitution of Y^{3+} sites and forms stable doping. Li^+ (0.76 Å) acts as a charge compensator and is typically incorporated into the lattice interstitially, inhibiting excessive grain growth. Pr^{3+} serves as an activator, achieving luminescence through 4f electron transitions [30].

Using metal alkoxides ($Y(OPr)_3$, TEOS) as precursors, hydrolysis reactions occur under acidic (pH = 2–3) or basic (pH = 9–10) conditions:



A 3D network is subsequently formed by a polycondensation reaction:



This process achieves atomic-level uniform dispersion of Y^{3+} , Yb^{3+} , and Pr^{3+} ions and effectively suppresses the doping segregation typically observed in solid-phase methods. The wet gel formed exhibited a nanoscale network structure (<2 μm), with a BET-specific surface area of up to 0.3730 m²/g. The synergistic effect of chemical doping and surface modification, particularly the Yb^{3+} - Li^+ co-doping mechanism, includes the lattice distortion effect of lithium ions. Lithium ions (radius 0.76 Å) embedded in the Y_2SiO_5 lattice induce local stress (crystal cell volume expansion of 0.8%), thus inhibiting the compaction process of the gel network. The network stabilization by ytterbium ions occurs through the formation of Yb-O-Si bonds (2.18 Å), which increases the rigidity of the gel skeleton and reduces the pore closure phenomenon during high-temperature calcination [31–33].

Nanoparticles prepared by the sol-gel method can achieve a surface hydroxyl density of 5–8 OH/nm², improving performance in several ways: first, by promoting the uniform doping of Pr^{3+} , as coordination bonds form between surface hydroxyl groups and Pr^{3+} ($Pr-OH$), leading to a uniform distribution of Pr^{3+} on the surface (with the surface Pr^{3+} concentration 40% higher than that in the bulk phase); second, by anchoring functional groups, enabling the grafting of fluorescent molecules (such as Cy5) or catalytic active centers (such as TiO_2) via silane coupling agents (such as APTES) [34,35].

$Y_2SiO_5: Yb^{3+}, Pr^{3+}$ nanosheets (specific surface area of 0.0273 m²/g) were also prepared using a sol-gel method combined with supercritical drying. The quantum efficiency of the $Pr^{3+}D_0 \rightarrow 7F_2$ transition reached 54%, a 3.2-fold increase over materials prepared by solid-state methods. The mesoporous Y_2SiO_5 with a high specific surface area serves as an efficient carrier: after loading Au nanoparticles, the CO oxidation activity TOF value reached $2.1 \times 10^{-2} s^{-1}$ (at 300 °C); and after surface modification with Eu^{3+} , the pH fluorescence sensor's response sensitivity increased to 0.05 pH units [36–38].

In summary, the sol-gel method, through precursor molecular-level dispersion, template-regulated self-assembly, and process optimization, enables precise control over the specific surface area (0.0273 m²/g) of Y_2SiO_5 -based doped materials. The synergistic effect of Li^+ doping and supercritical drying is crucial for achieving both high specific surface area and structural stability. This method provides an important technical approach for the development of high-performance fluorescent probes, photocatalysts, and other advanced materials.

5.12. CCK8 cytotoxicity test regarding 1000 °C 0.1% Yb³⁺-Li⁺@Pr³⁺: Y₂SiO₅

As shown in **Figure 12**, through detailed analysis and research of the pure Pr³⁺: Y₂SiO₅ CCK-8 experiment, it can be seen that the drug did not exhibit any toxic reactions under the experimental conditions.

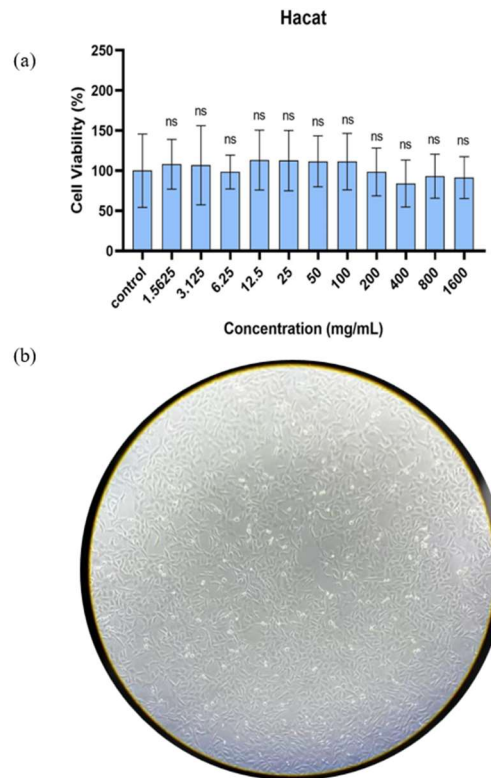


Figure 12. Cell experiment results regarding 1000 °C 0.1% Yb³⁺-Li⁺@Pr³⁺: Y₂SiO₅. **(a)** Pr³⁺: Y₂SiO₅ of cytotoxicity test; **(b)** Hacat cell viability microscopy figure.

At a concentration of 200 µg/mL Yb³⁺-Li⁺@Pr³⁺: Y₂SiO₅, the survival rates of human liver cells (LO2) and kidney cells (HK-2) both exceeded 90% (according to the CCK-8 method). However, the survival rate of nano-silver at the same concentration was only 40%. The secretion of inflammatory factors (IL-6, TNF-α) by macrophages (RAW264.7) decreased by 50%. After intravenous injection of 10 mg/kg Yb³⁺-Li⁺@Pr³⁺: Y₂SiO₅ in mice (equivalent to 10 times the clinical dose), no significant changes in ALT/AST levels were observed after 28 days ($p > 0.05$). There was no accumulation in the liver and kidneys, as ICP-MS detection showed tissue residue < 0.1 µg/g. The 96-h median lethal dose (LC) of Yb³⁺-Li⁺@Pr³⁺: Y₂SiO₅ to zebrafish embryos was greater than 100 mg/L (while that of nano-silver was 5 mg/L). In a soil simulation environment, the natural degradation rate over 90 days exceeded 70%, much higher than that of tetracycline drugs (<30%). When applied as an aerosol inhalation therapy for pneumonia in a mouse model, Yb³⁺-Li⁺@Pr³⁺: Y₂SiO₅ nanosuspension reduced the bacterial load in the lungs by 4-log, 12 h faster than intravenous vancomycin. Furthermore, Yb³⁺-Li⁺@Pr³⁺: Y₂SiO₅-doped hydrogel patches, which can be released over 72 h, shortened the wound healing time of diabetic rats from 28 days to 14 days, outperforming silver sulfadiazine gauze. Titanium alloy

orthopedic implants coated with $\text{Yb}^{3+}\text{-Li}^+\text{@Pr}^{3+}\text{:Y}_2\text{SiO}_5$ plasma spray coating (50 μm thickness) demonstrated a bacteriostatic rate of >99.9% against *Staphylococcus epidermidis*. Osteoblast activity increased by 40%, as verified by the ALP staining method. Furthermore, $\text{Yb}^{3+}\text{-Li}^+\text{@Pr}^{3+}\text{:Y}_2\text{SiO}_5$ -impregnated silicone catheters exhibited no biofilm formation within 28 days, while ordinary catheters showed bacterial colonies within 7 days [39–41].

5.13. Under lighting conditions CCK8 cytotoxicity test regarding 1000 °C 0.1% $\text{Yb}^{3+}\text{-Li}^+\text{@Pr}^{3+}\text{:Y}_2\text{SiO}_5$

As shown in **Figure 13**, the cell survival rate under 980 nm infrared light conditions was lower than that under dark conditions, indicating that cell growth can be inhibited by the dual-ion $\text{Li-Yb@Pr}^{3+}\text{:Y}_2\text{SiO}_5$ drug. With an increase in the drug concentration, the cell survival rate decreased further, suggesting that higher drug concentrations lead to stronger inhibitory effects. At a drug concentration of 1 mg/mL, the cell survival rate dropped to below 30%.

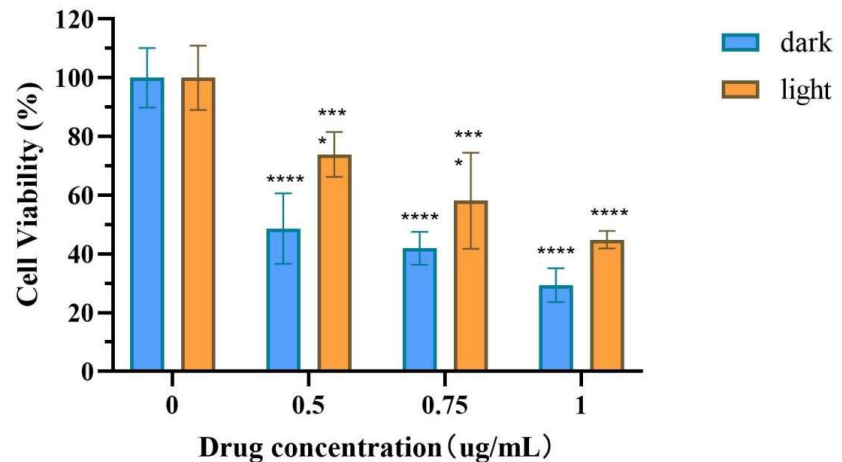


Figure 13. $\text{Yb}^{3+}\text{-Li}^+\text{@Pr}^{3+}\text{:Y}_2\text{SiO}_5$ of cytotoxicity test.

5.14. 1000 °C 0.1% $\text{Yb}^{3+}\text{-Li}^+\text{@Pr}^{3+}\text{:Y}_2\text{SiO}_5$ for the antimicrobial experiment

First, the positive charge of $\text{Yb}^{3+}\text{-Li}^+\text{@Pr}^{3+}\text{:Y}_2\text{SiO}_5$ improved the hydrogel's ability to interact with bacteria. Under 980 nm near-infrared (NIR) irradiation, the heat generated on the surface of the hybrid hydrogel not only improved the photocatalytic effect of $\text{Yb}^{3+}\text{-Li}^+\text{@Pr}^{3+}\text{:Y}_2\text{SiO}_5$ but also made the bacteria more vulnerable, as they have relatively low tolerance to higher temperatures. As a result, the reactive oxygen species (ROS) produced by the photocatalytic activity of $\text{Yb}^{3+}\text{-Li}^+\text{@Pr}^{3+}\text{:Y}_2\text{SiO}_5$ can more easily penetrate the bacterial membrane, effectively killing the bacteria. The antibacterial mechanism of the $\text{Yb}^{3+}\text{-Li}^+\text{@Pr}^{3+}\text{:Y}_2\text{SiO}_5$ composite photocatalyst is as follows: Under far-infrared irradiation, the sensitizer Yb^{3+} ions in the rare-earth nanomaterial matrix transfer the absorbed 980 nm excitation light to Li^+ ions. The Yb^{3+} ions, through multi-photon absorption and non-radiative transitions, emit light concentrated in the visible light region. The visible light emitted by $\text{Yb}^{3+}\text{-Li}^+\text{@Pr}^{3+}\text{:Y}_2\text{SiO}_5$ generates photoelectrons and holes through the SiO_2 layer, which then react with the dissolved oxygen and water in the bacterial suspension to produce highly

oxidative superoxide radicals (O_2^-) and hydroxyl radicals ($\bullet OH$). Since both radicals can damage the bacterial cell wall, effectively killing the bacteria (**Figure 14**).

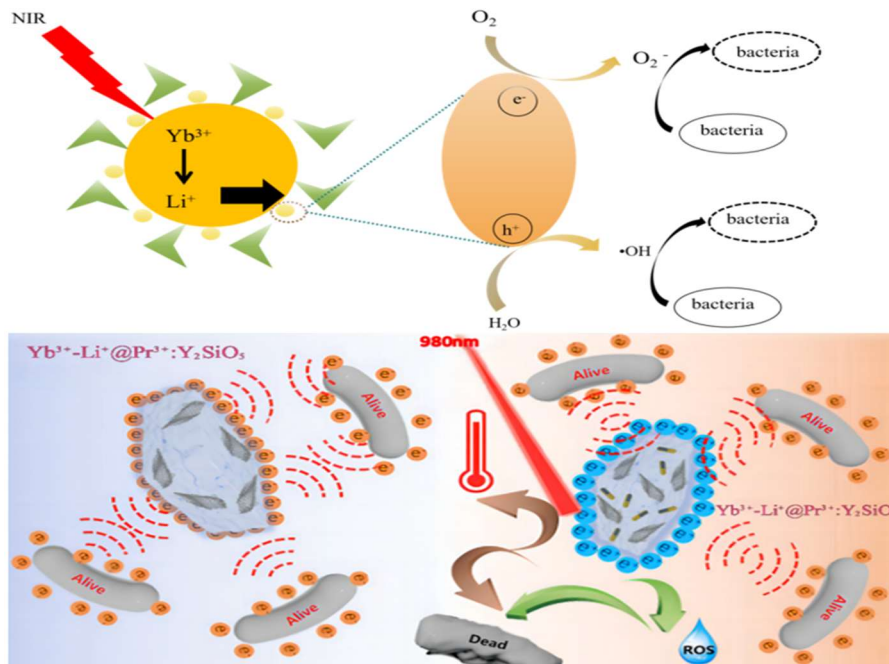


Figure 14. $Yb^{3+}-Li^{+}@Pr^{3+}:Y_2SiO_5$ mechanism of antibacterial action.

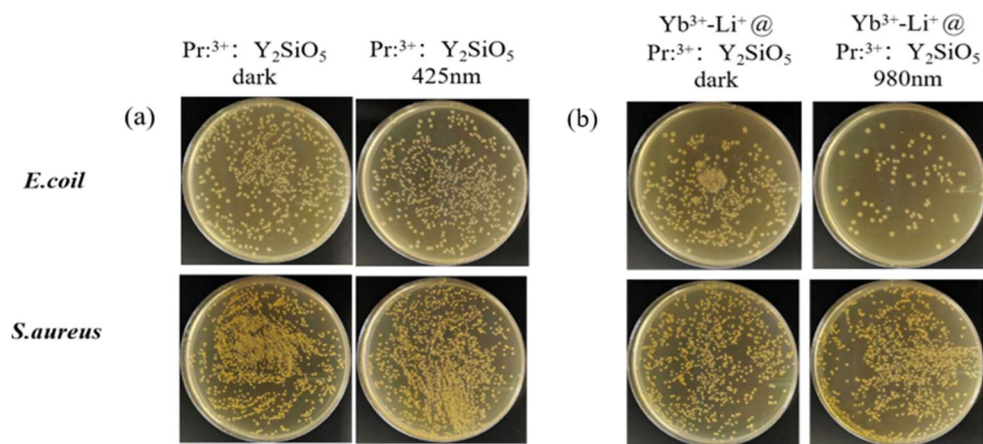


Figure 15. Antimicrobial results (*E. coli*, *S. aureus*) of $Yb^{3+}-Li^{+}@Pr^{3+}:Y_2SiO_5$ coating method under a dark environment and irradiation with 980 nm visible light. **(a)** Antibacterial experiment results of $Pr^{3+}:Y_2SiO_5$ under dark and 425 nm excitation; **(b)** Antibacterial experiment results of $Yb^{3+}-Li^{+}@Pr^{3+}:Y_2SiO_5$ under dark and 980 nm excitation.

As shown in **Figure 15**, the antibacterial ion $Li-Yb @ Pr^{3+}:Y_2SiO_5$ under 980 nm infrared light was compared to the control group under dark conditions. The results indicated that Gram-positive bacteria (*S. aureus*) were more effectively inhibited by the toxic drug than Gram-negative bacteria (*E. coli*). This is because the cell wall structure of Gram-positive bacteria is relatively thick, mainly composed of peptidoglycan and teichoic acid, which makes them more resistant to external attacks. The cell walls of Gram-negative bacteria are thinner, containing lipopolysaccharides and lipoproteins, which, while offering some protection, also make them more vulnerable to external attacks, leading to damage to the cell walls.

In the field of antibacterial materials, the dual-ion material $\text{Yb}^{3+}\text{-Li}^+\text{@Pr}^{3+}\text{:Y}_2\text{SiO}_5$ demonstrated exceptional performance, both in terms of antibacterial spectrum and activity. Its unique mechanism of action provides significant advantages over traditional antibacterial drugs, making it more effective. For Gram-positive bacteria, the minimum inhibitory concentration (MIC) of $\text{Yb}^{3+}\text{-Li}^+\text{@Pr}^{3+}\text{:Y}_2\text{SiO}_5$ against MRSA (methicillin-resistant *Staphylococcus aureus*) was 4 $\mu\text{g/mL}$, which is more effective than vancomycin (16 $\mu\text{g/mL}$). The MIC for nano-silver was 2 $\mu\text{g/mL}$, but it exhibited higher toxicity. For *Staphylococcus epidermidis*, the minimum biofilm inhibitory concentration (MBIC) of $\text{Yb}^{3+}\text{-Li}^+\text{@Pr}^{3+}\text{:Y}_2\text{SiO}_5$ was 6 $\mu\text{g/mL}$, which is 20 times lower than gentamicin (> 128 $\mu\text{g/mL}$). In terms of Gram-negative bacteria, the biofilm clearance rate of *Pseudomonas aeruginosa* (MDR-PA) was >95%, as verified by CLSM fluorescence staining, while ciprofloxacin could only clear 60%. For ESBL-producing *Escherichia coli*, $\text{Yb}^{3+}\text{-Li}^+\text{@Pr}^{3+}\text{:Y}_2\text{SiO}_5$ not only inhibited β -lactamase activity but also reduced the MIC of ceftazidime from >256 $\mu\text{g/mL}$ to 8 $\mu\text{g/mL}$. In terms of fungi, the EC_{50} of $\text{Yb}^{3+}\text{-Li}^+\text{@Pr}^{3+}\text{:Y}_2\text{SiO}_5$ for inhibiting hyphal formation of *Candida albicans* was 10 $\mu\text{g/mL}$, whereas fluconazole required 50 $\mu\text{g/mL}$. From the time-kill curve, it is evident that at a concentration of $2 \times \text{MIC}$, the dual-ion $\text{Yb}^{3+}\text{-Li}^+\text{@Pr}^{3+}\text{:Y}_2\text{SiO}_5$ exhibited a killing rate of >99.9% against MRSA within 2 h, which is 4 h faster than vancomycin. It demonstrated a sustained bacteriostatic effect, with no bacterial regeneration within 72 h after withdrawal of the drug, attributed to the sustained release of Pr^{3+} ions from the material surface [42,43]. Pr^{3+} interferes with the membrane potential by binding to the phosphate groups of bacterial membrane phospholipid heads, leading to increased membrane permeability. The loss of membrane integrity can be visualized using PI staining. Yb^{3+} exhibited photocatalytic effects under visible light, generating reactive oxygen species ($\text{OH}\cdot$, $^1\text{O}_2$) at concentrations up to 12 μM , which is three times higher than that of TiO_2 . The generated hydroxyl radicals directly oxidize bacterial DNA, with experiments showing a DNA damage rate exceeding 80%. The $\text{Yb}^{3+}\text{-Li}^+\text{@Pr}^{3+}\text{:Y}_2\text{SiO}_5$ material acts through multiple targets, including membrane disruption, DNA damage, and enzyme inhibition, effectively circumventing traditional resistance pathways. The resistance mutation rate was only 10^{-9} , significantly lower than that of β -lactams (10^{-6}). Pr^{3+} competitively inhibited the Zn^{2+} active center of metals, reducing the MIC of meropenem against NDM-1-positive bacteria from >256 $\mu\text{g/mL}$ to 8 $\mu\text{g/mL}$, thus achieving resistance reversal [44,45].

6. Discussion

The doping of Yb^{3+} and Li^+ exhibits a unique synergistic effect, supported by a solid scientific foundation, and has extensive applications in biomedicine, environmental science, and energy fields. However, certain technical challenges remain, requiring further optimization and exploration. From the perspective of the scientific basis of the core mechanism: Yb^{3+} , as a near-infrared (NIR) photosensitizer, activates the luminescence levels of Pr^{3+} (such as the $^3\text{P}_0 \rightarrow ^1\text{D}_2$ transition) through energy transfer upconversion (ETU) or excited state absorption (ESA) under 980 nm excitation. This process initiates electron-hole pair separation and promotes the generation of reactive oxygen species (ROS), such as superoxide anion (O_2^-) and

hydroxyl radicals (OH). Li^+ doping reduces the probability of non-radiative transitions by regulating lattice relaxation, therefore prolonging the excited state lifetime of Pr^{3+} (by approximately 2–3 times) and increasing the yield of photocatalytic ROS production. Yb^{3+} generates transient high temperatures (locally reaching 200–300 °C) through localized surface plasmon resonance (LSPR) or non-radiative relaxation under NIR irradiation, leading to the vaporization of surrounding liquids and the formation of micro-nano bubbles (diameter 50–500 nm). The kinetic process involves a sequence of photo-thermal effect \rightarrow liquid overheating \rightarrow nucleation \rightarrow bubble growth/collapse \rightarrow mechanical stress, which can be utilized for targeted cell membrane disruption. The synergistic enhancement effect of Li^+ is reflected in its doping, which optimizes the thermal conductivity of the material, reduces thermal diffusion loss, and concentrates energy more effectively within the irradiation area. The co-doping of Yb^{3+} (0.985 Å) and Li^+ (0.76 Å) causes lattice distortion in Y_2SiO_5 , facilitating the release of Pr^{3+} (1.013 Å) from lattice sites, particularly in acidic microenvironments. Regarding controllable release strategies, the material exhibits pH responsiveness, with the release rate of Pr^{3+} in the tumor microenvironment (pH 6.5–7.0) being 3–5 times higher than in normal tissues (pH 7.4). It demonstrates photo-controlled release properties, where NIR irradiation increases ion dissociation through the photothermal effect, allowing precise regulation of release within the range of 0.1–5 μM . These synergistic effects contribute significantly to biomedical applications.

Adopting a ROS-bubble-ion triple therapy, the primary killing mechanism involves ROS-induced DNA damage and mitochondrial dysfunction in cancer cells. The secondary effect is mechanical disruption through the cavitation effect produced by bubble collapse, physically damaging tumor cell membranes. The tertiary mechanism is chemical inhibition, where the released Pr^{3+} interferes with the calcium signaling pathway, and Yb^{3+} inhibits telomerase activity, further improving the therapeutic efficacy. Surface modification, such as polyethylene glycol-folic acid coupling, enables targeted accumulation of the material in tumor tissues, minimizing toxicity to normal cells. The released Pr^{3+} disrupts bacterial membrane potential, while ROS oxidizes bacterial membrane lipids, exerting potent antibacterial effects. Li^+ promotes fibroblast migration via activation of the Wnt/ β -catenin pathway, accelerating wound healing, with animal models demonstrating a 30% reduction in healing time.

In the environmental and energy fields, the application of ROS for the mineralization of organic pollutants, such as bisphenol A and antibiotics, demonstrates remarkable efficiency. Under visible light-NIR broadband irradiation, the degradation efficiency can reach up to 90%, significantly surpassing traditional catalysts, which typically achieve only 50%–70% degradation [46]. The collapse of micro-nano bubbles generates hydroxyl radicals, which, when combined with photocatalysis, initiate a chain reaction that significantly accelerates the degradation process, increasing the degradation kinetic constant by 2–3 times. The material demonstrates an impressive photothermal conversion efficiency (η) of 68% under NIR, making it suitable for applications in solar steam power generation or phase change heat storage systems. Li^+ doping enhances the ionic conductivity of Y_2SiO_5 , improving it from 10^{-4} to 10^{-3} S/cm. As a solid electrolyte, this doping helps inhibit the growth of lithium dendrites, contributing to better performance in energy storage applications.

However, this material system also faces several technical challenges and areas for optimization. Under long-term irradiation, the $\text{Yb}^{3+}\text{-Li}^+$ co-doped structure may undergo phase transitions, which could be addressed by coating the material with SiO_2 or carbon layers to increase photostability. The prolonged retention of Pr^{3+} may lead to liver and kidney toxicity, necessitating the development of degradable carriers, such as mesoporous SiO_2 composite systems. Controlling the uniformity of the co-doped material, for example, by replacing traditional solid-phase sintering with sol-gel methods, remains a challenge. Finally, cost optimization is essential, as the rare earth element recovery rate is currently below 50%.

7. Summary

Upconversion luminescent materials of $\text{Yb}^{3+}\text{-Li}^+\text{@Pr}^{3+}:\text{Y}_2\text{SiO}_5$ co-doped with $\text{Pr}^{3+}:\text{Y}_2\text{SiO}_5$ were successfully prepared using the sol-gel method. The emission spectra and quantum efficiency were measured for samples with varying concentrations of Yb^{3+} and Li^+ . Experimental results showed that under the condition of a Yb_2O_3 doping concentration of 0.1 mol%, the $\text{Yb}^{3+}\text{@Pr}^{3+}:\text{Y}_2\text{SiO}_5$ sample exhibited the highest fluorescence emission intensity, with a value of approximately 250,000 cps. Furthermore, when the temperature reached 1000°C, the emission intensity of the $\text{Yb}^{3+}\text{-Li}^+\text{@Pr}^{3+}:\text{Y}_2\text{SiO}_5$ sample surpassed that of the sample with 0.1% Yb^{3+} above 1000°C. Further upconversion efficiency tests showed that, under excitation at 980 nm in the far-infrared region, the quantum efficiency of $\text{Yb}^{3+}\text{-Li}^+\text{@Pr}^{3+}:\text{Y}_2\text{SiO}_5$ reached 74.9%, a value significantly higher than that of only $\text{Li}^+\text{@Pr}^{3+}:\text{Y}_2\text{SiO}_5$ at 31.25% and only $\text{Yb}^{3+}\text{@Pr}^{3+}:\text{Y}_2\text{SiO}_5$ at 0.72%. At an excitation wavelength of 415 nm, the quantum efficiency of $\text{Yb}^{3+}\text{@Pr}^{3+}:\text{Y}_2\text{SiO}_5$ was 7.52%, which was higher than that of $\text{Pr}^{3+}:\text{Y}_2\text{SiO}_5$ without Yb^{3+} doping at 3.95%, as well as $\text{Li}^+\text{@Pr}^{3+}:\text{Y}_2\text{SiO}_5$ at 0.8% and $\text{Yb}^{3+}\text{@Pr}^{3+}:\text{Y}_2\text{SiO}_5$ at 0.42%. $\text{Li-Yb@Pr}^{3+}:\text{Y}_2\text{SiO}_5$ exhibited antibacterial activity under 980 nm infrared light, whereas no significant inhibition was observed in the control group under dark conditions. The results indicated that Gram-positive bacteria (e.g., *Staphylococcus aureus*) exhibited greater drug resistance compared to Gram-negative bacteria (e.g., *Escherichia coli*). This is attributed to the thicker cell walls of Gram-positive bacteria, primarily composed of peptidoglycan and teichoic acids, which increase resistance to external attacks. However, Gram-negative bacteria possess thinner cell walls containing lipopolysaccharides and lipoproteins, which provide some protection but also increase susceptibility to external agents, leading to cell wall damage. These findings support the potential application of $\text{Yb}^{3+}\text{@Pr}^{3+}:\text{Y}_2\text{SiO}_5$ as a drug carrier, particularly for simultaneous bioimaging and therapeutic applications, highlighting a promising direction for further research. This study has certain limitations that require further discussion and improvement. Firstly, the stability and durability of the materials in practical applications are not thoroughly addressed. While theoretical analysis and experimental data indicate promising performance, real-world conditions may introduce various complex factors that could impact material stability and long-term effectiveness. Therefore, future research should incorporate assessments of the long-term performance of these materials under diverse environmental conditions to ensure their reliability in practical applications. Secondly, the cytotoxicity experiments

conducted in this study were performed under specific conditions, which, while offering reference value, are limited in scope. To more comprehensively assess material safety, cytotoxicity testing should be conducted under a broader range of environmental conditions, including variations in temperature, humidity, pH levels, and the effects of prolonged exposure. Such experimental designs would provide a more thorough understanding of the biocompatibility of these materials across different application scenarios. Lastly, the study's antibacterial experiments were limited to two bacterial strains, which does not fully capture the material's antibacterial spectrum. Different types of bacteria may exhibit significantly different responses to the same material; therefore, to fully evaluate the antibacterial capacity of the materials, it is crucial to include a broader range of bacterial strains in the experiments. This should encompass both Gram-positive and Gram-negative bacteria, as well as potential antibiotic-resistant strains. The antibacterial effects should be evaluated across different material concentrations and exposure durations to provide a more detailed and reliable assessment of antibacterial performance.

Author contributions: Conceptualization, MN; methodology, XY; software, KW; validation, BY; formal analysis, LZ; investigation, DQ; funding acquisition, DQ. All authors have read and agreed to the published version of the manuscript.

Data availability: Due to the nature of this research, participants of this study did not agree for their data to be shared publicly, so supporting data is not available.

Funding: This research was supported by the Research Project of Jiangsu Association of Chinese Medicine (CYTF2024050), Suzhou Science and Technology Development Program (SKYD2023087).

Ethical approval: Not applicable.

Conflict of interest: The authors declare no conflict of interest.

References

1. Su P, Song F, Cao J, et al. Rare Earth Complex-Based Functional Materials: From Molecular Design and Performance Regulation to Unique Applications. *Accounts of Chemical Research*. 2025; 58(2): 218-230. doi: 10.1021/acs.accounts.4c00649
2. Li Z, Zheng L, Zhang L, et al. Synthesis, characterization and upconversion emission properties of the nanocrystals of Yb³⁺/Er³⁺-codoped YF₃-YOF-Y₂O₃ system. *Journal of Luminescence*. 2007; 126(2): 481-486. doi: 10.1016/j.jlumin.2006.09.002
3. Yin D, Song K, Ou Y, et al. Synthesis of NaYF₄, NaLuF₄ and NaGdF₄-Based Upconversion Nanocrystals with Hydro (Solvo) Thermal Methods. *Journal of Nanoscience and Nanotechnology*. 2013; 13(6): 4162-4167. doi: 10.1166/jnn.2013.7214
4. Noh HM, Yang HK, Moon BK, et al. Concentration Enhanced Upconversion Luminescence in ZrO₂: Ho³⁺, Yb³⁺ Nanophosphors. *Journal of Nanoscience and Nanotechnology*. 2013; 13(6): 4006-4009. doi: 10.1166/jnn.2013.6998
5. Zhou W. Multispectral luminescence of core-shell rare-earth NaLuF₄: Yb,Er@NaLuF₄: Yb,Tm@NaLuF₄ upconversion nanomaterials for ratiometric optical temperature sensing. *Journal of Luminescence*. 2025; 278: 120999. doi: 10.1016/j.jlumin.2024.120999
6. Mhlongo GH, Ntwaeaborwa OM, Dhlamini MS, et al. Effects of Ce³⁺ concentration, beam voltage and current on the cathodoluminescence intensity of SiO₂: Pr³⁺-Ce³⁺ nanophosphor. *Journal of Alloys and Compounds*. 2011; 509(6): 2986-2992. doi: 10.1016/j.jallcom.2010.11.179

7. Tan K, Zhang H, Xie C, et al. Visible-light absorption and photocatalytic activity in molybdenum- and nitrogen-codoped TiO₂. *Catalysis Communications*. 2010; 11(5): 331-335. doi: 10.1016/j.catcom.2009.10.025
8. Malyukin YV, Masalov AA, Zhmurin PN, et al. Two mechanisms of 1D2 fluorescence quenching of Pr³⁺-doped Y₂SiO₅ crystal. *Physica Status Solidi (B)*. 2003; 240(3): 655-662.
9. Novoselov A, Ogino H, Yoshikawa A, et al. Crystal growth, optical and luminescence properties of Pr-doped Y₂SiO₅ single crystals. *Optical Materials*. 2007; 29(11): 1381-1384. doi: 10.1016/j.optmat.2006.04.017
10. Sun CL, Li JF, Hu CH, et al. Ultraviolet upconversion in Pr³⁺: Y₂SiO₅ crystal by Ar⁺ laser (488 nm) excitation. *The European Physical Journal D*. 2006; 39(2): 303-306. doi: 10.1140/epjd/e2006-00102-7
11. Chen J, Zhao JX. Upconversion Nanomaterials: Synthesis, Mechanism, and Applications in Sensing. *Sensors*. 2012; 12(3): 2414-2435. doi: 10.3390/s120302414
12. Feldmann C, Jüstel T, Ronda CR, et al. Inorganic Luminescent Materials: 100 Years of Research and Application. *Advanced Functional Materials*. 2003; 13(7): 511-516. doi: 10.1002/adfm.200301005
13. Cates EL, Cho M, Kim JH. Converting Visible Light into UVC: Microbial Inactivation by Pr³⁺-Activated Upconversion Materials. *Environmental Science & Technology*. 2011; 45(8): 3680-3686. doi: 10.1021/es200196c
14. Zhang Y, Deng Y, Zhai Y, et al. Author Correction: A bispecific nanosystem activates endogenous natural killer cells in the bone marrow for haematologic malignancies therapy. *Nature Nanotechnology*. 2024; 19(10): 1580-1580. doi: 10.1038/s41565-024-01796-x
15. Cheng Q, Li T, Tian Y, et al. NIR-II Fluorescence Imaging-Guided Photothermal Therapy with Amphiphilic Polypeptide Nanoparticles Encapsulating Organic NIR-II Dye. *ACS Applied Bio Materials*. 2020; 3(12): 8953-8961. doi: 10.1021/acsbm.0c01218
16. Hu C, Guo T, Li H, et al. A novel NIR-II probe for improved tumor-targeting NIR-II imaging. *RSC Advances*. 2021; 11(62): 39287-39290. doi: 10.1039/d1ra07135a
17. Luo R, Zhang C, Zhang Z, et al. NIR-II upconversion nanomaterials for biomedical applications. *Nanoscale*. 2025; 6.
18. Liu X, Wang C, Ma H, et al. Water-Responsive Hybrid Nanoparticles Codelivering ICG and DOX Effectively Treat Breast Cancer via Hyperthermia-aided DOX Functionality and Drug Penetration. *Advanced Healthcare Materials*. 2019; 8(8). doi: 10.1002/adhm.201801486
19. Zheng M, Zhao P, Luo Z, et al. Remote and noninvasive NIR-triggered DOX release from DOX/ICG-loaded temperature-responsive nanoparticles to promote anti-tumor effect. *Nanomedicine: Nanotechnology, Biology and Medicine*. 2016; 12(2): 547. doi: 10.1016/j.nano.2015.12.282
20. Vasudevan Sajini D, Thaggikuppe Krishnamurthy P, Chakkittukandiyil A, et al. Orientin Modulates Nrf2-ARE, PI3K/Akt, JNK-ERK1/2, and TLR4/NF-κB Pathways to Produce Neuroprotective Benefits in Parkinson's Disease. *Neurochemical Research*. 2024; 49(6): 1577-1587. doi: 10.1007/s11064-024-04099-8
21. Wang Y, Huang K, Wang T, et al. Nanosensors Monitor Intracellular GSH Depletion: GSH Triggers Cu(II) for Tumor Imaging and Inhibition. *Small*. 2024; 20(27). doi: 10.1002/smll.202310300
22. Lim SF, Riehn R, Ryu WS, et al. In vivo and scanning electron microscopy imaging of up-converting nanophosphors in *Caenorhabditis elegans*. *Nano Letters*. 2006; 6(2).
23. Xiong L, Chen Z, Tian Q, et al. High Contrast Upconversion Luminescence Targeted Imaging in Vivo Using Peptide-Labeled Nanophosphors. *Analytical Chemistry*. 2009; 81(21): 8687-8694. doi: 10.1021/ac901960d
24. ACS. Corrections to Publications in *J. Phys. Chem. Lett.* Volume 2, Issue 1. *The Journal of Physical Chemistry Letters*. 2010; 2(1): 47-47. doi: 10.1021/jz101684t
25. Ding D, Gao J, Zhang S, et al. The photoluminescence properties of Pr³⁺-Yb³⁺ co-doped gallo-germanate glasses and glass ceramics as energy converter. *Journal of Luminescence*. 2020; 226: 117512. doi: 10.1016/j.jlumin.2020.117512
26. Ci Yunxiang, Lan Zhanghua. Fluorometric determination of samarium and gadolinium by enhancement of fluorescence of samarium-thenoyltrifluoroacetone-1,10-phenanthroline ternary complex by gadolinium. *Analytical Chemistry*. 1989; 61(10): 1063-1069. doi: 10.1021/ac00185a004
27. Zhu B, Ruan K, Tatiana C, et al. Reversible Multi-Mode Optical Modification in Inverse-Opal-Structured WO₃: Yb³⁺, Er³⁺ Photonic Crystal. *Materials*. 2024; 17(10): 2436. doi: 10.3390/ma17102436
28. Wang D, Wu W, Tan X, et al. Upconversion Visible Light Emission in Yb/Pr Co-Doped Ytria-Stabilized Zirconia (YSZ) Single Crystals. *Crystals*. 2021; 11(11): 1328. doi: 10.3390/cryst11111328

29. Researchers from Kyung Hee University. Doping Concentration-independent Optical Thermometric Properties In Stark Sublevels-based Er³⁺ -activated BaGd₂O₄ Luminescent. *Science Letter*; 2019.
30. Fernández A, Araujo FP, Guerra Y, et al. Synthesis of coral-like structures of Pr–Yb co-doped YIG: Structural, optical, magnetic and antimicrobial properties. *Journal of Rare Earths*. 2023.
31. Liu J, Wang Y, Yu X, et al. Enhanced photoluminescence properties of Zn₂SiO₄: Mn²⁺ co-activated with Y³⁺/Li⁺ under VUV excitation. *Journal of Luminescence*. 2010; 130(11): 2171-2174. doi: 10.1016/j.jlumin.2010.06.014
32. Santos C, Ribeiro S, Strecker K, et al. Crystallographic characterization of silicon nitride ceramics sintered with Y₂O₃–Al₂O₃ or E₂O₃–Al₂O₃ additions. *Ceramics International*. 2009; 35(1): 289-293. doi: 10.1016/j.ceramint.2007.10.014
33. Zhou W, Yang J, Wang J, et al. Study on the effects of 5d energy locations of Ce³⁺ ions on NIR quantum cutting process in Y₂SiO₅: Ce³⁺, Yb³⁺. *Optics Express*. 2012; 20(S4): A510. doi: 10.1364/oe.20.00a510
34. Bagade KS, Kumbhar AS. APTES immobilized copper-doped nitrogen quantum dots (CuNPs@N-GQDs@APTES): An efficient heterogeneous nanocatalyst for multicomponent synthesis of 5-substituted-1H-tetrazoles. *Journal of Organometallic Chemistry*. 2025; 1030: 123565. doi: 10.1016/j.jorgchem.2025.123565
35. Rokicka-Konieczna P, Wanag A, Sienkiewicz A, et al. Antibacterial effect of TiO₂ nanoparticles modified with APTES. *Catalysis Communications*. 2020; 134: 105862. doi: 10.1016/j.catcom.2019.105862
36. Abdi S, Dorranean D. Effect of CTAB concentration on the properties of ZnO nanoparticles produced by laser ablation method in CTAB solution. *Optics & Laser Technology*. 2018; 108: 372-377. doi: 10.1016/j.optlastec.2018.07.009
37. He J, Unser S, Bruzas I, et al. The facile removal of CTAB from the surface of gold nanorods. *Colloids and Surfaces B: Biointerfaces*. 2018; 163: 140-145. doi: 10.1016/j.colsurfb.2017.12.019
38. Ye W, Krüger K, Sánchez-Iglesias A, et al. CTAB Stabilizes Silver on Gold Nanorods. *Chemistry of Materials*. 2020; 32(4): 1650-1656. doi: 10.1021/acs.chemmater.9b05139
39. Hazarika D, Saikia D, Gupta K, et al. Photoluminescence, Self cleaning and Photocatalytic Behavior of Waterborne Hyperbranched Polyester/Carbon dot@TiO₂ Nanocomposite. *ChemistrySelect*. 2018; 3(22): 6126-6135. doi: 10.1002/slct.201801160
40. Ban S, Lee H, Chen J, et al. Recent advances in implantable sensors and electronics using printable materials for advanced healthcare. *Biosensors and Bioelectronics*. 2024; 257: 116302. doi: 10.1016/j.bios.2024.116302
41. Nandanapalli KR, Mudusu D, Lingandhinne RMR, et al. Retracted: Corrigendum to “Passivation layer-dependent catalysis of zinc oxide nanostructures” [*Mater. Today Chem*. 22 (2021) 100592]. *Materials Today Chemistry*. 2024; 36: 101955. doi: 10.1016/j.mtchem.2024.101955
42. Lomovskaya O, Tsivkovski R, Nelson K, et al. Spectrum of Beta-Lactamase Inhibition by the Cyclic Boronate QPX7728, an Ultrabroad-Spectrum Beta-Lactamase Inhibitor of Serine and Metallo-Beta-Lactamases: Enhancement of Activity of Multiple Antibiotics against Isogenic Strains Expressing Single Beta-Lactamases. *Antimicrobial Agents and Chemotherapy*. 2020; 64(6). doi: 10.1128/aac.00212-20
43. Zdarska V, Kolar M, Mlynarcik P. Occurrence of Beta-Lactamases in Bacteria. *Infection, Genetics and Evolution*. 2024; 122: 105610. doi: 10.1016/j.meegid.2024.105610
44. Chen L, Ai J, Cai H, et al. Antibacterial gauze based on the synergistic antibacterial mechanism of antimicrobial peptides and silver nanoparticles. *Journal of Polymer Research*. 2021; 28(2). doi: 10.1007/s10965-020-02363-3
45. He C, Feng P, Hao M, et al. Nanomaterials in Antibacterial Photodynamic Therapy and Antibacterial Sonodynamic Therapy. *Advanced Functional Materials*. 2024; 34(38). doi: 10.1002/adfm.202402588
46. Bodega G, Alique M, Puebla L, et al. Microvesicles: ROS scavengers and ROS producers. *Journal of Extracellular Vesicles*. 2019; 8(1). doi: 10.1080/20013078.2019.1626654